We are IntechOpen,
the world's leading publisher of
Open Access books
Built by scientists, for scientists

6,300
Open access books available

171,000
International authors and editors

190M
Downloads

154
Countries delivered to

Our authors are among the

TOP 1%
most cited scientists

12.2%
Contributors from top 500 universities

CLARIVATE ANALYTICS

BOOK CITATION INDEX

INDEXED

WEB OF SCIENCE™

Selection of our books indexed in the Book Citation Index
in Web of Science™ Core Collection (BKCI)

Interested in publishing with us?
Contact book.department@intechopen.com

Numbers displayed above are based on latest data collected.
For more information visit www.intechopen.com

Electrostatic Discharge, Electrical Overstress, and Latchup in VLSI Microelectronics

Steven H. Voldman

Abstract

Electrostatic discharge (ESD), electrical overstress (EOS), and latchup have been an issue in devices, circuit and systems for VLSI microelectronics for many decades and continue to be an issue till today. In this chapter, the issue of ESD, EOS and latchup will be discussed. This chapter will address some of the fundamental reasons decisions that are made for choice of circuits and layout. Many publications do not explain why certain choices are made, and we will address these in this chapter. Physical models, failure mechanisms and design solutions will be highlighted. The chapter will close with discussion on how to provide both EOS and ESD robust devices, circuits, and systems, design practices and procedures. EOS sources also occur from design characteristics of devices, circuits, and systems.

Keywords: electrical overstress, electrostatic discharge, latchup, system failure, component failure

1. Introduction

Electrostatic discharge (ESD) and electrical overstress (EOS) have been an issue with electrical systems even prior to semiconductors and VLSI technology [1–25]. With the scaling of semiconductor components, ESD continues to be a manufacturing and design issue [2], while latchup also became a reliability and design issue with the introduction of CMOS technology [1–25].

In this chapter, we will address why certain choices and circuit directions are made. This chapter will hopefully provide some insight from a person who has done extensive work in the ESD design and chip development.

In electronic design, a plethora of electrical events can occur. **Figure 1** illustrates the type of topics including ESD, EOS, latchup as well as electromagnetic interference (EMI), and electromagnetic compatibility (EMC). In this chapter, the focus will only be on ESD, EOS, and latchup.

2. Qualification of semiconductor components—electrostatic discharge (ESD)

ESD is a common form of component level failure and system level from manufacturing, shipping, and handling. Historically, the ESD sources in manufacturing
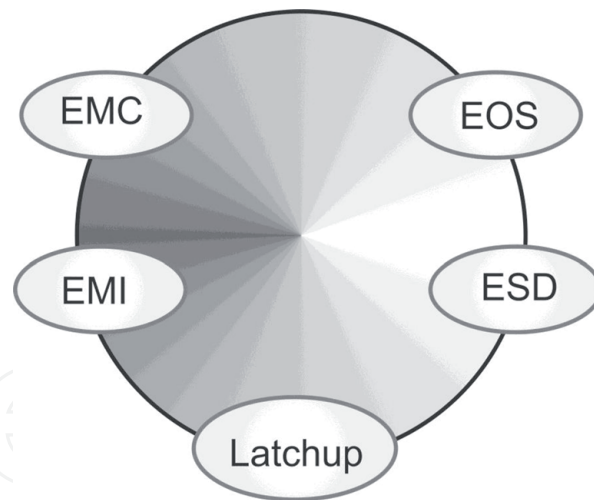
Figure 1.
ESD, EOS, latchup, EMI and EMC.

exceeded the ESD robustness of products leading to component failures. Significant improvements in manufacturing environments as well as ESD solutions in circuit design reduced the concern of component failure levels for many years. Manufacturing charging occurred due to inadequate ionization, material properties, and charging processes from cutting, etching, and dicing. Today, the ESD models performed for qualification and shipping of semiconductor components are as follows [4]:

- human body model (HBM); and

- charged device model (CDM).

With the introduction of VLSI microelectronics, additional qualification of components includes [4]:

- latchup; and

- transient latchup.

CMOS latchup was a large concern in space applications. For low power, CMOS technology was introduced into high density VLSI products. The chapter will address the successes and mistakes made in the industry that lead to latchup failures.

2.1 The human body model (HBM)

Today, the human body model (HBM) is the most established standard for the reliability of components in the semiconductor industry [2–4, 6]. The HBM test is integrated into the qualification and release process of the quality and reliability teams for components in corporations and foundries [6] and is fundamental in the semiconductor chip development cycle.

The human body model (HBM) is regarded as an electrostatic discharge (ESD) event, not an electrical overstress (EOS) event [1–11]. The human body model (HBM) represents a model of a human beings electrical discharge to a semiconductor component. The model assumes that the human being is charged and discharges to the component.

Additionally, HBM failures occur in the power rails and the ESD "power clamps" between the power rails. HBM failures can occur in digital, analog, or radio frequency applications. The failure signature is typically isolated to a single device, or a few elements. HBM failures occur for both positive and negative polarity discharges.

ESD circuits respond to a specific pulse width to mitigate the ESD pulse event. ESD circuits guide the ESD current away from the signal path and to an "alternate current path" through the power grid and ESD power clamp. ESD circuits are "tuned" to be responsive to specific pulse widths.

HBM ESD failures can occur in the following:

• MOSFET active devices;

• diode active devices;

• bipolar junction transistors (BJT) devices;

• resistor passive elements;

• capacitor passive elements;

• inductor passive elements;

• interconnect wiring;

• Vias;

• contacts;

• power rails; and

• decoupling capacitors.

The key question is what is the best choice for providing ESD protection that

• achieves good ESD robustness;

• does not impact circuit functionality;

• does not a reliability concern;

• wide application space for many different designs; and

• migratable to the next technology without significant changes or re-work.

ESD events can be of positive or negative polarity. ESD events can be singular polarity or oscillatory. As a result, ESD protection networks must be able to address both polarity types. In an oscillatory pulse, the positive current flows through the alternate current path through the VDD power grid, and for negative polarity, current flows through the VSS power grid. Additionally, they remain off during normal functional operation of a semiconductor chip.

An example of an ESD protection network is a dual-diode network [3]. The dual-diode ESD network is a commonly used network for complimentary metal

oxide semiconductor (CMOS) technology because it has the following essential features:

- low turn-on voltage;

- low capacitance;

- responds to both positive and negative polarity events;

- remains off during functional operation.;

- migratable technology to technology; and

- small area required.

For ESD engineers and technologists, a large advantage of the dual-diode ESD network is that it is easy to migrate from one technology generation to another technology generation. For corporations that used MOSFETs for ESD protection strategies, they generate a large amount of work to be successful, and many times, they are unsuccessful. With MOSFET ESD networks, there is not a scalable strategy that guarantees migration from one generation to another.

Additionally, in CMOS technology, the shallow trench isolation (STI) structure is scalable. In CMOS technology with STI isolation, the breakdown voltage does not change with STI scaling but remains a constant. This allows for suitable migration without issues and without failure or re-work.

The second key advantage is that it has a low turn-on voltage of 0.7 V. The low turn-on voltage allows for discharge of the current through the alternate current loop and redirects the current away from the signal path. The third advantage is that it can be designed with low capacitance, making it suitable for CMOS, advanced CMOS, and RF technologies; this minimizes the impact to chip performance. The fourth advantage is that it does not contain MOSFET gate dielectric failure mechanisms. Unlike MOSFET ESD protection solutions, there is no dielectric, and hence no dielectric failure mechanisms.

A commonly used ESD networks is the grounded gate n-channel MOSFET device [3]. As the technology scales, the MOSFET snapback voltage reduces, leading to an earlier turn-on of the MOSFET. Unfortunately, the dielectric breakdown and overstress are problems in this circuit. Hence, although used in many applications, it is limited in migration to advanced technologies.

A commonly used ESD power clamp is the RC-triggered ESD MOSFET power clamp. Why is it widely used?

- Early turn-on based on the frequency dependent transient impulse from an ESD event.

- Establishes alternate current loop away from the signal path.

- Works well in conjunction with ESD double-diode network on the input node.

- Circuit impedance scales with the MOSFET width in the RC-triggered clamp.

The reason is that the RC-triggered ESD MOSFET power clamp turns on the MOSFET in response to an HBM ESD event. This RC-triggered clamp responds to

the ESD current in the power rail leading to turn-on of the MOSFET as opposed to MOSFET breakdown. This element works well with the ESD double-diode network that is used on the signal pins. Additionally, this circuit scales with MOSFET width, and is not dependent on MOSFET second breakdown response.

2.2 Charged device model (CDM)

The charged device model (CDM) is an electrostatic discharge (ESD) test method that is part of the qualification of semiconductor components. The charged device model (CDM) event is associated with the charging of the semiconductor component substrate and package. The charging of the package occurs through direct contact charging, or field-induced charging process (e.g., the field induced charge device model (FICDM)).

The charged device model (CDM) pulse is regarded as the fastest event of all the ESD events [4, 12–15]. Note that the CDM pulse waveform is influenced by the test platform and measurement metrology.

The CDM event has a significantly different characteristic from the HBM event, and requires different ESD circuit solutions. First, the CDM event is oscillatory. Second, the discharge is fast.

CDM event damage occurs in the semiconductor chip through the substrate. It can also occur through the power supply. Charge is stored on the package and the substrate; then, the power supply rapidly discharges through the grounded pin. Since the charge storage is through the entire substrate, it is distributed phenomena and hence spatially dependent. The CDM failure mechanism can be small "pin-hole" in a MOSFET gate structure; this can occur in receiver networks, as well as metal interconnects.

The current path for charged device model (CDM) in components is significantly different from other electrostatic discharge (ESD) events. In the case of the charged device model (CDM), the package and/or chip substrate is charged through a power or ground rail. The component itself is charged slowly to a desired voltage state. As a result, the current flows from the component itself to the grounded pin during ESD testing. This is significantly from other ESD tests (e.g., HBM events) that ground a reference and then apply an ESD event to a signal or power pin. As a result, the current path that a CDM event follows is from inside the component to the pin that is grounded during test.

3. Qualification of semiconductor components—electrical overstress (EOS)

A second area of interest is electrical overstress (EOS). Electrical overstress (EOS) has been an issue in devices, circuits, and systems for VLSI microelectronics for many decades, as early as the 1970s, and continues to be an issue today [1]. Due to a wide variety of pulse events, slow progress has been made at improving EOS robustness.

Electrical overstress (EOS) sources exist from natural phenomena and power distribution [1, 14–25]. Switches, cables, and other power electronics can be a source of electrical overstress. EOS sources exist in devices, circuits, and systems.

3.1 Safe operating area

Figure 2 illustrates the safe operating area (SOA) of a semiconductor device. There is a current limit and a voltage limit on the borders of the SOA. At the corner of the
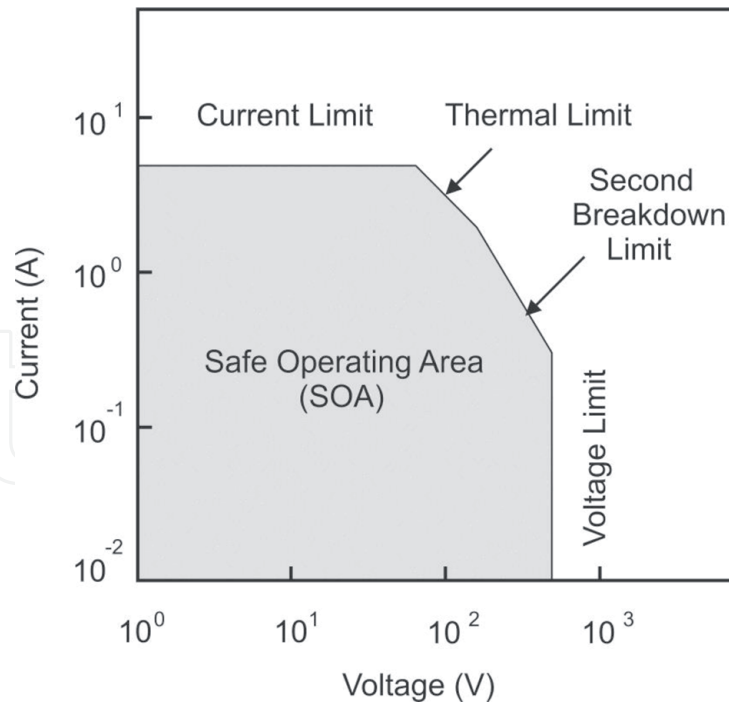
Figure 2.
Safe operating area (SOA).

SOA, the limitation is a thermal limit and a second breakdown limit. The thermal limit has to do with the thermal capacity of a semiconductor device prior to failure. Second breakdown has to do with thermal breakdown limit of a device prior to failure.

Electrical over-voltage (EOV), electric over-current (EOC), and electrical over-power (EOP) can lead to failure mechanisms; these can lead to melted packages, blown single component capacitors and resistors, ruptured packages, blown bond wires, cracked dielectrics, fused and melted metal layers, and molten silicon.

3.2 EOS failure mechanisms

Visual external or internal inspection can be applied to evaluate EOS failure mechanisms. Visual damage signatures can include package lead damage, foreign material, cracks, discoloration, and corrosion. Visual damage can also be evaluated from internal inspection. For internal inspection, visual damage signatures are melted metallurgy, cracked inter-level dielectrics, and molten silicon.

There are certain categories of failures that electrostatic discharge (ESD) does not typically cause and EOS events do cause. Failures that are typically caused by EOS phenomena but not ESD include printed circuit board (PCB), package pin, and wire bond damage.

3.3 EOS protection devices

Electrical overstress (EOS) protection devices are supported by a large variety of technology types. Although the material and device operations may differ between the EOS protection devices, the electrical characteristics can be classified into a few fundamental groups [16–25].

EOS protection networks can be identified depending on whether it is suppressing voltage, as a voltage suppression device, or the current, as a current-limiting device. The voltage suppression device limits the voltage magnitude observed on the signal pins, or power rails of a component, preventing electrical over-voltage (EOV). The current-limiting device prevents a high current from reaching sensitive nodes, hence avoiding electrical over-current (EOC) [1].

Voltage suppression devices can also be sub-divided into two major classifications [1]. Voltage suppression devices can be segmented into devices that remain with a positive differential resistance region and those that undergo a negative resistance region. For a positive differential resistance, these devices can be referred to as "voltage clamp" devices where dI/dV remains positive for all states. For the second group, there exists a region where dI/dV is negative. The first group can be classified as "voltage clamp devices," whereas the second group can be referred to as an "S-type I-V characteristic device," or as a "snapback device." In the classification of voltage suppression devices, the second classification can be associated with the directionality; a voltage suppression device can be "uni-directional" or "bi-directional."

The choice of electrical overstress (EOS) device to use in an application is dependent on the parameters, such as electrical characteristics, cost, and size. The electrical characteristics that are of interest are the breakdown voltage and the forward conduction [1].

The types of voltage suppression devices used electrical overstress (EOS) include transient voltage suppression (TVS) diodes [22], thyristor devices, varistor devices [21], polymer voltage suppression (PVS) devices, and gas discharge tube (GDT) devices [23]. Current-limiting devices can be used in a series configuration for electrical overstress (EOS) protection [16–24]. The choice of the current-limiting EOS protection device is a function of the cost, size, rated current, time response, I^2t value, rated voltage, voltage drops, and application requirements.

4. CMOS latchup

Latchup is a condition where a semiconductor device undergoes a high current state as a result of interaction of a pnp and a npn bipolar transistor [5]. The pnp and npn transistors can be natural to the technology, or parasitic devices. In CMOS technology, these are typically parasitic devices.

When interaction occurs between a pnp and a npn bipolar transistor, or parasitics of CMOS transistors, regenerative feedback between the two transistors can lead to electrical instability. When the two transistors, parasitic or non-parasitic are coupled, the combined device acts as a four-region device of alternating p- and n-doped regions with three physical p-n metallurgical junctions, forming a pnpn structure. When these parasitic pnpn elements undergo a high current state, latchup can initiate thermal runaway and can be destructive.

Latchup events can lead to destruction of a semiconductor chip, package, or system.

There are many reasons why latchup is an issue in today's semiconductor chips. The reason why it is a concern in some corporations differs based on the choices made in the semiconductor technology, latchup design strategy, as well as the latchup methodology.

These are just some of the reasons why today CMOS latchup is not "cured" and remains an issue in today's semiconductor chips. In this text, we will address many of these issues in the future chapters.

5. Conclusions

In conclusion, significant advancements have been made in the understanding of ESD, EOS, and latchup failure mechanisms, as well as solutions to address them have been applied in semiconductor electronics.

Author details

Steven H. Voldman
IEEE Fellow, United States of America

*Address all correspondence to: voldman@ieee.org

IntechOpen

References

[1] Voldman S. Electrical Overstress (EOS): Devices, Circuits, and Systems. Chichester: Wiley; 2013

[2] Voldman SESD. Physics and Devices. Chichester: Wiley; 2004

[3] Voldman S. ESD: Circuits and Devices. 2nd ed. Chichester: Wiley; 2015

[4] Voldman S. ESD Testing: From Components to Systems. Chichester: Wiley; 2016

[5] Voldman S. Latchup. Chichester: Wiley; 2007

[6] ANSI/ESD ESD-STM 5.1. ESD Association Standard Test Method for the Protection of Electrostatic Discharge Sensitive Items - Electrostatic Discharge Sensitivity Testing - Human Body Model (HBM) Testing - Component Level. Standard Test Method (STM) Document; 2007

[7] Guest PG, Sikora VW, Lewis B. Bureau of Mines, Report of Investigation 4833. Washington, D.C: U.S. Department of Interior; 1952

[8] Bulgin D. Static electrification. British Journal of Applied Physics, Suppl 2. 1953. DOI: 19.1088/0508-3443/4/s2/333

[9] Martin C. Duration of the Resistive Phase and Inductance of Spark Channels. Atomic Weapons Research Establishment, SSWA/JCM/1065/25. 1996;7:287-293

[10] Hyatt H, Calvin H, Mellberg H. A closer look at the human ESD event. In: Proceedings of the Electrical Overstress/Electrostatic Discharge (EOS/ESD) Symposium. Rome, New York: ESD Association; 1981. pp. 1-8

[11] Hyatt H, Calvin H, and Mellberg H. Bringing ESD into the 20th century. In: Proceedings of the IEEE International Electromagnetic Compatibility (EMC) Symposium; 1982

[12] ANSI/ESD ESD-STM 5.3.1. ESD Association Standard Test Method for the Protection of Electrostatic Discharge Sensitive Items - Electrostatic Discharge Sensitivity Testing – Charged Device Model (CDM) Testing - Component Level. Standard Test Method (STM) Document. Rome, New York: ESD Association; 1999

[13] JEDEC. JESD22-C101-A. A Field-Induced Charged Device Model Test Method for Electrostatic Discharge-Withstand Thresholds of Microelectronic Components; 2000

[14] Renninger R, Jon M, Lin D, Diep T, Welsher T. A field-induced charged device model simulator. In: Proceedings of the Electrical Overstress/Electrostatic Discharge (EOS/ESD) Symposium. Rome, New York: ESD Association; 1989. pp. 59-71

[15] Renninger RG. Mechanisms of charged device electrostatic discharges. In: Proceedings of the Electrical Overstress/Electrostatic Discharge (EOS/ESD) Symposium. Rome, New York: ESD Association; 1991. pp. 127-143

[16] Edison TA. Fuse Block. Washington, D.C: USPTO; US Patent No. 438,305. October 14, 1890

[17] Page CG. Improvement in Induction-Coil Apparatus and in Circuit Breakers. US Patent No. 76,654; 1868

[18] Wright A, Newbury PG. Electric Fuses. 3rd ed. Piscatewey, New Jersey: Institute of Electrical Engineers; 2004. pp. 2-10

[19] Kraz V. Origins of EOS in manufacturing environment. In:

Proceedings of the Electrical Overstress/
Electrostatic Discharge (EOS/ESD)
Symposium. Rome, New York: ESD
Association; 2009. pp. 44-48

[20] Kaschani KT, Gaertner R. The
impact of electrical overstress on the
design, handling and application of
integrated circuits. In: Proceedings of
the Electrical Overstress/Electrostatic
Discharge (EOS/ESD) Symposium;
2011. pp. 220-229

[21] Philipp HR, Levinson LM. Transient
protection with ZnO varistors: Technical
considerations. In: Proceedings of the
Electrical Overstress/Electrostatic
Discharge (EOS/ESD) Symposium.
Rome, New York: ESD Association;
1980. pp. 26-34

[22] Hopkins DC. Protective level
comparisons for voltage transient
suppressors. In: Proceedings of the
Electrical Overstress/Electrostatic
Discharge (EOS/ESD) Symposium.
Rome, New York: ESD Association;
1980. pp. 35-43

[23] Bazarian A. Gas tube surge arresters
for control of transient voltages. In:
Proceedings of the Electrical Overstress/
Electrostatic Discharge (EOS/ESD)
Symposium. Rome, New York: ESD
Association; 1980. pp. 44-53

[24] Horgan EL. Analytical assessment
of electrical overstress effects on
electronic systems. In: Proceedings of
the Electrical Overstress/Electrostatic
Discharge (EOS/ESD) Symposium.
Rome, New York: ESD Association;
1980. pp. 140-148

[25] Durgin DL. An overview of
the sources and effects of electrical
overstress. In: Proceedings of the
Electrical Overstress/Electrostatic
Discharge (EOS/ESD) Symposium.
Rome, New York: ESD Association;
1980. pp. 154-160

We are IntechOpen,
the world's leading publisher of
Open Access books
Built by scientists, for scientists

6,300
Open access books available

171,000
International authors and editors

190M
Downloads

154
Countries delivered to

Our authors are among the

TOP 1%
most cited scientists

12.2%
Contributors from top 500 universities

WEB OF SCIENCE™

Selection of our books indexed in the Book Citation Index
in Web of Science™ Core Collection (BKCI)

Interested in publishing with us?
Contact book.department@intechopen.com

Numbers displayed above are based on latest data collected.
For more information visit www.intechopen.com

Chapter

Development and Characterization of Poly Ethylene-Co-Vinyl Acetate (PEVA) Hybrid Nanocomposite Encapsulates for Solar PV

Rashmi Aradhya, Madhu Bilugali Mahadevaswamy and Poornima

Abstract

In the solar photo voltaic (PV) module, encapsulant material provides the environmental protection, insulation, optical absorption, besides serving as a good adhesive between solar cell and components of PV module for improving the efficiency. It is desired to develop an improved encapsulating material by incorporating the light absorbing inorganic nanofillers in thermoplastic polymers. One such matrix material is poly ethylene-co-vinyl acetate (PEVA), finding its importance in solar materials, such as PV modules and agricultural greenhouse polymer sheets. Inorganic nanofillers have the potential to transmit necessary radiance in the UV spectra, which can improve the PV panel efficiency. In this study, the optimum effect of inorganic fillers such as organically modified montmorillonite clay (OMMT) and titanium dioxide (TiO_2) anatase in PEVA matrix is observed. The fabricated nanocomposite films were etched from the glass mold. The morphology and miscibility of fabricated nanocomposite films were analyzed and investigated by scanning electron microscopy (SEM), X-ray diffraction technique (XRD), UV-Vis absorption (UV-Vis), and Fourier-Transform Infrared Spectroscopy (FTIR). The dielectric properties of the fabricated hybrid nanocomposite films were analyzed for its insulation behavior. The thermal behavior was studied using Thermo-gravimetric Analysis (TGA) and Differential Scanning Calorimetry (DSC). The hybrid nanocomposite with 5.0 weight percentage (wt.%) OMMT and 5.0 weight percentage (wt.%) of TiO_2 indicates lowest dielectric constant of 2.4 and marginal increase in dissipation factor with respect to frequency. Increased thermal stability, glass transition temperature, high transmittance and optimum UV-shielding efficiency were found with the same wt.% in the proposed work.

Keywords: characterization, hybrid nanocomposites, poly ethylene-co-vinyl acetate, solar encapsulant, thermo-gravimetric analysis, X-ray diffraction technique

1. Introduction

The necessity to increase the energy generation is to meet the present day scenario of increasing energy demand, environmental pollution and decline in the nonrenewable energy sources. This has led to the explore of various renewable energy resources [1]. Even though renewable energy sources has appeared to be the

best possible solution in terms of sustainability, portability, and availability, it is not commercially feasible in short period of time as compared to conventional fuels. This is due to complex processing technologies and material supply limitations. The solar

The photovoltaic (PV) provides pure and renewable alternative energy source, potentially advantageous to the environment by preventing greenhouse gases being generating and go into the atmosphere. The PV industry is increasing quickly as the demand for cleaner energy worldwide continues to increase.

As the industry develops, it is significant that suitable materials are available to meet the several requirements such as robustness, performance, cost and global availability.

Silicone materials have been used in a wide variety of applications in industries, such as construction and electronics industries, and perfect product to meet the requirements in the PV module assembly market.

In order to achieve best possible performance, the encapsulant material used in the development of photovoltaic modules should satisfy a number of requirements, which include: high optical transmittance of incident light, good dielectric properties (thermally conductive and electrically insulating), good mechanical strength to protect the PV cells from outside mechanical loads and thermal stresses, good adhesion to both glass and PV cells, and sufficiently robust to survive 20–30 years in the field. This paper provides the overview and the key requirements for materials as PV encapsulants. In the recent developments of hybrid materials, both organic-inorganic nanofillers are receiving major attention due to broad range of potential applications [2].

PEVA, as used in the solar industry, is a thermoplastic elastomer that is formulated with a curing agent, UV absorbers, as well as photo and thermo-antioxidants. Even though, PEVA encapsulation meets largely the rigorous material property necessity at an attractive price, there exists a couple of areas for improvement.

Composites of PEVA reinforced with OMMT and TiO_2 nanofillers have emerged as a key field of research because of numerous advantages, which includes an improvement in mechanical, dimensional, thermal properties and enhanced transparency when dispersed nanoclay platelets suppress polymer crystallization [3]. Even at very low weight percentage of the nanofiller addition, capable to alter properties of the polymer present in nanocomposite compared to the pristine polymer because the bulk of polymer chains positioned such that they are in close contact with the OMMT surface. OMMT has outer tetrahedral layers that contain Si^+ and O^- atoms. These outer layers align themselves due to Van der Waals forces of attraction between them to form nonionic bond [4].

Nanocomposites developed using organic polymer and inorganic nanofillers forms a new set of materials with confirmation of improved performance when compared with their macroscopic counterparts [5]. The nanocomposite film developed combines the unique properties of inorganic components with the processability of polymer in one material and makes them attractive in varieties of useful applications [6]. Polymers are considered to be most appropriate accommodating matrices for composite materials because they can be easily tailored by adding inorganic filler which has long-term stability and good processability to suit the variety of physical properties. Inorganic nanofillers exhibit better optical, catalytic, electronic and magnetic properties, which are considerably different from their bulk states. The addition of inorganic nanofillers to the polymer matrix allows unique physical properties as well as the implementation of new end-user features. Depending on the particle size, particle shape, specific surface area and chemical nature of the nanofillers, intended polymer matrix properties can be modified [7]. A good cross-linking agent is required for better interactions between the polymer

matrix and the nanofillers, as it is directly linked to morphology, crystallinity, photothermal stability, shelf life and thermal stability and also it affects the curing rate by generating the free radical through thermal decomposition [8, 9].

In the present work, pristine PEVA and nanocomposite films with OMMT and TiO_2 as nanofillers with dicumyl peroxide as a curing agent were fabricated by solution casting technique which is found to the optimized fabrication method. From the exhaustive literature review, it was also concluded that dicumyl peroxide is the optimized curing agent for EVA polymer and synthesis of nanocomposite films [10–12].

The nanocomposite films were characterized by Fourier Transform Infrared spectroscopy (FTIR), X-ray diffraction (XRD), Thermogravimetric analysis (TGA), UV-Vis spectroscopy, scanning electron microscopy (SEM) and electrical parameters with LCR meter. The interaction between EVA and OMMT and TiO_2 nanofillers was investigated and the results demonstrate the doping effect of OMMT and TiO_2 nanofillers. The objective of the study carried out to determine the effects of OMMT and TiO_2 nanofillers on PEVA polymer and to investigate introduction of inorganic TiO_2 nanofiller will influence dispersion of the nanoparticles in the polymer matrix for encapsulant application in solar PV modules with improved thermal stability, dielectric properties and optimum UV-shielding efficiency. In the present work, the investigations were carried out on the electrical, thermal and morphological properties of OMMT and TiO_2 nanofillers added in PEVA.

2. Experimental

### 2.1 Materials

The base matrix material used is poly (ethylene-co-vinyl acetate) vinyl acetate 25 wt.%, melt index 19 g/10 min (190°C/2.16 kg), contains 200–900 ppm BHT as an inhibitor. Nanofillers such as nanoclay (montmorillonite clay) surface modified: 25–30 wt.% trimethyl stearyl ammonium and titanium (IV) oxide-anatase (nanopowder, <25 nm particle size, 99.7% trace metals basis). Dicumyl peroxide 98% bis (α-dimethyl benzyl) peroxide is added to the composite as a curing agent. All materials were supplied by Sigma-Aldrich Pvt. Ltd., Bangalore. Toluene with 98% purity used to dissolve the polymer and nanofillers were procured from Karnataka Fine Chem., Bangalore.

2.2 Composites sample preparation

The good dispersion is a key challenge to achieve the best possible combination of matrix nanoparticles. For that reason, a new dispersion technique, such as ultra-sonication, was followed by manual mixing with different mixing speed and time. This processing method was optimized because it was not very complicated from laboratory processing point of view and commercially available polymers and nanoparticles could be mixed easily and ease to prepare a composite sample. The agglomeration of nanosized particles was significantly reduced with this mixing technique resulting in a well dispersed and homogeneous mixture of nanocomposites.

Pristine PEVA with curing agent dicumyl peroxide (DCP) doped with OMMT and TiO_2 nanofillers, at different concentrations were prepared by the solution casting method as shown in **Figure 1**. Initially, the PEVA solution was prepared by weighing the appropriate amount of PEVA and dissolving it in toluene at 45°C with the help of magnetic stirrer for 45 min and for the solution 2, 5, 7 wt.%,
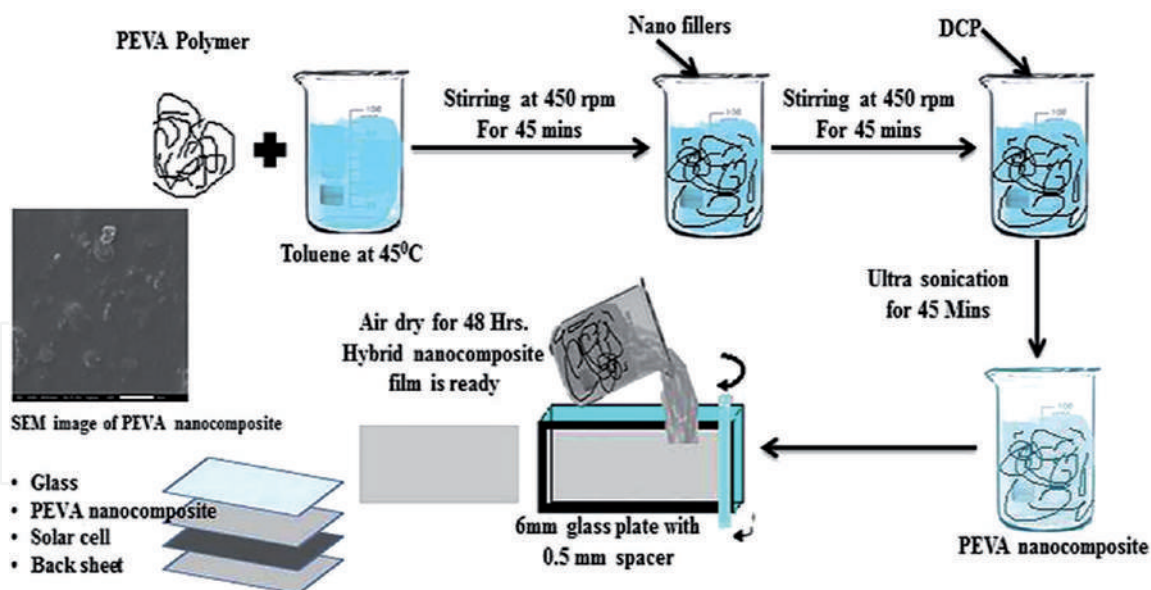
Figure 1.
Process followed for making composite films.

of OMMT and TiO_2 nanofillers, were mixed and stirred vigorously by using a magnetic stirrer until it is uniformly dispersed, a clear multi-component PEVA dispersion was obtained. Further, curing agent was added to the solution and ultra-sonication was carried out for 45 min to achieve the complete dispersion of nanofillers in PEVA solution. Appropriate mixtures of PEVA and nanofillers solution were poured on to the clean glass plate and left to dry at room temperature for about 24 h. The fabricated nanocomposites were post cured for 48 h in a hot air oven at 45°C then the nanocomposite films were removed from the glass plate and cut into required sizes for characterization. The thickness of the obtained composite films was measured using a digital micrometer at different places and average value was taken.

2.3 Characterization

Electrical parameters measurement were carried out for pure PEVA and PEVA nanocomposite samples by using fully automated high-precision four-terminal LCR meter (HIOKI-IM3536) and a four-terminal probe (HIOKIL2000) in the frequency range from 10 Hz to 4 MHz at a room temperature. The capacitance (c), dissipation factor (tanδ) and ac resistance were recorded directly and from which the dielectric constant (ε') and dielectric loss (ε'') were calculated.

The surface morphology of the PEVA and PEVA nanocomposite samples has been observed and recorded by using a scanning electron microscopy (SEM (JEOL, JSM-ITLV model)) with an accelerating voltage of 10 kV. Surface fractured samples were gold coated before making the observations.

XRD analysis of the nanocomposite films was carried out using powder X-ray diffractometer (Shimadzu-7000 with Cu-Kα radiation). Fourier Transform Infrared Spectra (FTIR) was recorded from the FTIR (Bruker-alpha) and analyzed for metal oxide bond stretching. The UV absorbance spectrum of the samples was measured using the Agilent Cary 60, Version 2.00, UV-Vis spectrophotometer with the scan rate of 60 (nm/min) with dual beam mode.

The thermal stability of nanocomposite films was analyzed using a thermo-gravimetric analyzer, TA Instrument, Q600, with a heating rate of 10°C/min with a temperature ranging from 30 to 800°C in the nitrogen gas atmosphere. The formulation and identification of the samples are listed in **Table 1**.

Sample identification and formulation	PEVA + DCP (wt.%)	OMMT (wt.%)	TiO$_2$ (wt.%)
PEVA + DCP	100	—	—
PEVA + DCP + 5 wt.% OMMT	95	5	—
PEVA + DCP + 5 wt.% OMMT + 5 wt.% TiO$_2$	90	5	5

Table 1.
Sample identification and formulation.

3. Results and discussion

3.1 XRD analysis

X-ray diffraction spectrum analysis is useful technique to evaluate the intercalation and exfoliation layered structure arrangement of OMMT and TiO$_2$ nanofillers in the PEVA base polymer matrix. **Figure 2** shows the complete XRD spectrum obtained for the nanocomposite samples from 5 to 50°. The shift in the characteristics peak of PEVA indicates the existence of good bonding between the nanofillers and pristine PEVA matrix [13]. Diffraction patterns obtained from fabricated PEVA + 5 wt.% OMMT + 5 wt.% TiO$_2$ nanocomposite showed broader peaks at lower value (6.44°) and at higher value (25.68°), suggesting intercalation/exfoliation of PEVA molecules into the intergallery spacing of OMMT. Peaks with similar diffraction patterns reported in the literature [3, 14] confirmed the good bonding between fillers and the polymer. XRD pattern also indicates the semi-crystalline/amorphous nature of the nanocomposite films. From the characteristics peaks, using Bragg's law, d-spacing can be calculated. From the result, it was observed that prominent diffraction peak obtained with OMMT nanofiller at 2θ = 6.47°, correspondingly intergallery d-spacing varies from 18.5 to 24.7 Å [15, 16] and for TiO$_2$ anatase [17, 18] diffraction peak occurred in the wide angle range of 2θ ascertained that the peaks at 25.36° shows crystalline structures of anatase synthesized TiO$_2$ nanoparticles. The complete or higher degree of exfoliation of layered crystalline structure of nanofillers in polymer matrix indicates the absence of corresponding peaks in the XRD spectra of the nanocomposite samples. The absence of peaks obtained from the XRD spectrum may be due to several reasons: Firstly, a very small or low concentration of the nanofillers in the regions, where X-ray beams scans the materials and secondly, loss of symmetry in certain crystallographic direction.

3.2 Scanning electron microscopy

Figure 3(a)–(c) shows the SEM images of PEVA, PEVA + DCP + 5 wt.% OMMT and PEVA + DCP + 5 wt.% OMMT + 5 wt.% TiO$_2$ nanocomposite films.
From the **Figure 3(b)** and **(c)**, it was found that the nanofillers were uniformly distributed and good adhesion between PEVA polymer and nanofillers. From the observation of surfaces in SEM micrographs **Figure 3(c)**, the possible agglomeration of TiO$_2$ nanofiller was ruled out and confirms the well-dispersed nanofillers in the PEVA polymer matrix. The characteristic peaks corresponding to OMMT and TiO$_2$ present in the XRD pattern of the nanocomposite films, referred to **Figure 2** supports a well-structured nanocomposite formation.

3.3 Fourier Transform Infrared Spectra (FTIR) analysis

Figure 4 shows the FTIR spectrum obtained by transmittance technique to find the different functional groups present and the interactions among nanofillers,
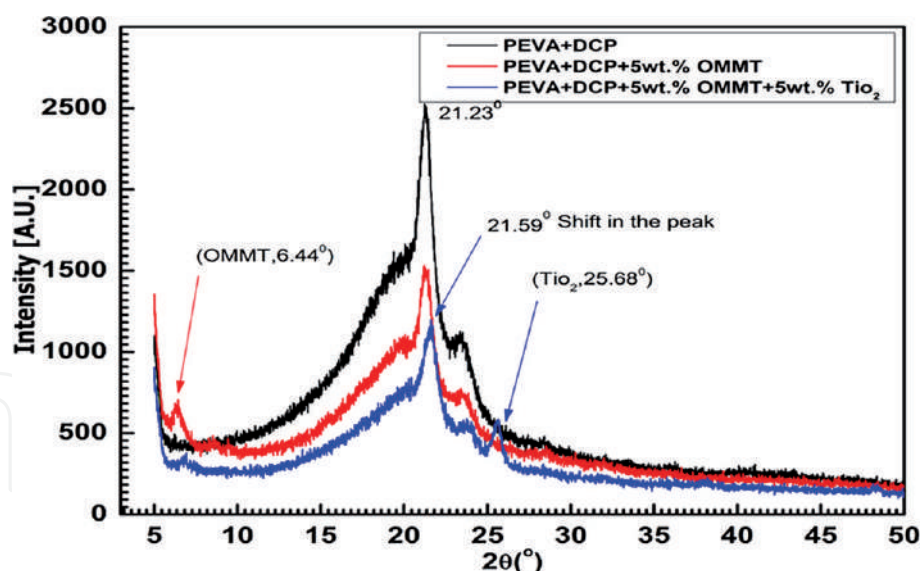
Figure 2.
XRD spectra of PEVA, PEVA + OMMT + TiO₂ nanocomposites.
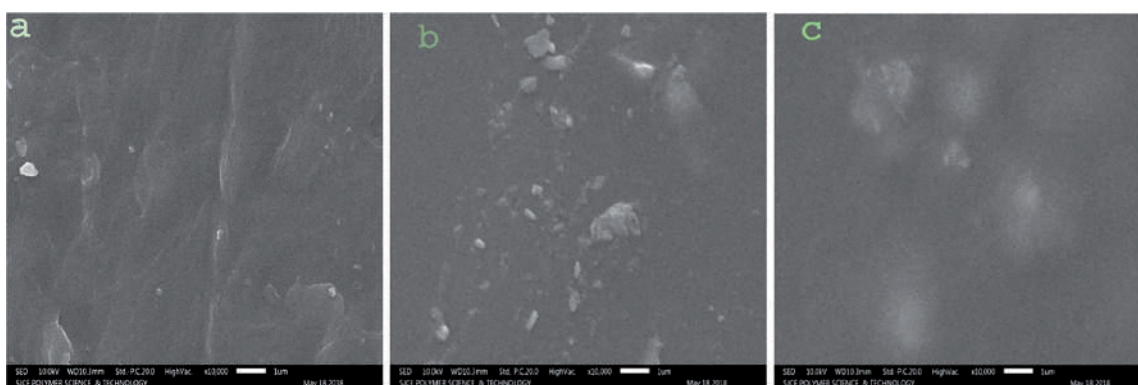
Figure 3.
SEM image of: (a) PEVA + DCP, (b) PEVA + DCP + 5 wt.% OMMT, and (c) PEVA + DCP + OMMT + TiO₂ nanocomposites.

curing agent and PEVA matrix. The effects of OMMT + TiO$_2$ nanofillers on the molecular structure and crystallization behavior of the PEVA composites can also be investigated. The FTIR spectrum of PEVA + OMMT + TiO$_2$ composite films shows the presence of the characteristic peaks of pure PEVA and pure OMMT and TiO$_2$. However, there is a relative shifting of the transmittance bands with increasing nanofillers content, due to hydrogen bonding interactions between -CH$_3$ groups of PEVA.

The FTIR spectra of nanocomposite films show the characteristic transmittance bands of pristine PEVA and OMMT + TiO$_2$ nanofillers. It was observed that the pre-dispersing procedure carried out in the preparation of the nanocomposite can considerably alter the morphology of the pure PEVA. The transmittance value of nanocomposite films found to be increased from 400 to 900 cm^{-1} as compared with the neat PEVA sample. The peaks at 720.55, 609.38, 514.67, and 463.15 cm^{-1} belongs to the characteristic peaks of OMMT + TiO$_2$ nanofillers, which are caused due to stretching vibrations and flexural vibration of O-Ti-O. The absorption peaks at around 1646 cm^{-1} and the wide peaks at around 2950.14 cm^{-1} are associated to flexural vibration of H-O-H bonds of physical inclusion of water and surface Ti-OH bonds and hydrogen bonded molecular water species respectively. This result indicates that a large number of -OH groups were absorbed on the surface of OMMT + TiO$_2$ nanofillers, which forms hydrogen bonds with the PEVA. In

PEVA + DCP + 5 wt.% OMMT + 5 wt.% TiO_2 sample has the stretching vibration of hydroxyl (-OH) group at 3456 cm^{-1}, indicating its hydrolyzation into silanol with hydroxyl (-OH) group. The stretching vibration of vinyl C=C appeared at 1600 cm^{-1}, out-of-plane wagging peak of vinyl CH_2 at 962 cm^{-1}, and the characteristic peak of the Si-O bond at 463.15 cm^{-1}. The abundance amount of free -OH groups are available on the nanoparticle surface and the density of hydrogen bonded PEVA segments will be high at the region just close to the nanoparticle surface. This process of formation of hydrogen bonds in the PEVA nanocomposite indicates the formation of two nanolayer; the tightly and strong nanolayer of PEVA segment at interface region with nanoparticles (**Table 2**).

3.4 UV-Vis spectroscopy

UV-Vis spectroscopy is used to understand the optical response of a polymer and nanocomposites when subjected to the absorption of UV-Vis radiation of the electromagnetic spectrum. In commonly used greenhouse covers and solar PV encapsulant, the thermal conductive and electrically insulative fillers are used to improve insulating properties which tends to reduce the transmission of visible
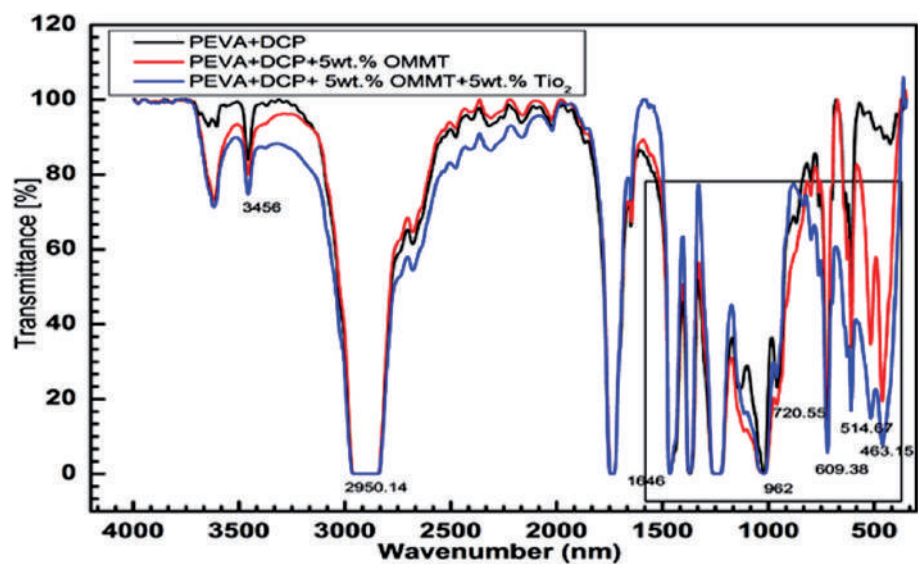
Figure 4.
FTIR spectra of PEVA + OMMT + TiO₂ nanocomposites.

Wave number (cm^{-1})	Functional groups
463.15	O-Ti-O
514.67	
609.38	
720.55	
962	Vinyl CH_2
1600	Vinyl C=C
1646	H-O-H
2950.14	H-O-H
3456	-OH

Table 2.
FTIR peaks corresponding to the functional groups.

light through the film. The ultraviolet and visible infrared spectra obtained for nanocomposite films are shown in **Figure 5**. It could be elucidated from the spectrum that it has a higher transparency/lower absorbance window between 200 and 800 nm. Absorption peaks are noticed between 200 and 280 nm for all samples. As the OMMT nanofiller is added, it is observed that the intensity of the absorption is augmented. The vertical axis shows the absorbance indicating the amount of light absorbed by the samples. The higher value in the vertical axis indicates the quantity of particular wavelength being absorbed.

They confirmed a decrease in UV transmission of PEVA and retained a high visible light transmission. Therefore, these nanocomposite films with light selective properties would be an excellent component for PV encapsulation. Among the nanocomposite films, the high absorption is observed below 230 nm which is not taken into consideration because of the large absorption coefficient of C=O bonds due to $\pi \rightarrow \pi^*$ transition (absorbance value exceeded 2, below 230 nm). Nanocomposite film with 5 wt.% OMMT and 5 wt.% TiO_2 allowed the maximum transmission of light and performs better.

3.5 Thermogravimetric analysis (TGA)

Thermo-gravimetric analysis (TGA) is usually used to understand the thermal stability behaviors of polymeric materials. Thermo gravimetric analysis (TGA) is finding increasing applications for investigations on the pyrolysis and combustion behavior of polymers. When a sample is subjected to TGA, decomposition occurs at a very slow rate until a critical temperature is reached. The pyrolysis rate then increases very rapidly to a maximum, leading to complete combustion and then the rate drops rapidly. Such a behavior is characteristic of a large number of decomposition processes, including pyrolysis of many polymers.

The TGA graph of fabricated nanocomposite samples shown in **Figure 6**.

The thermal degradation of EVA shows two distinct phases, which have been assigned to the loss of acetic acid and the degradation of the resulting unsaturated material. It consists of a combination of deacetylated vinyl acetate or unsaturated entities and ethylene entities of PEVA. From the literature, it was found that, as the process of deacetylation continues, inert degradation of polyene, oxidative degradation of
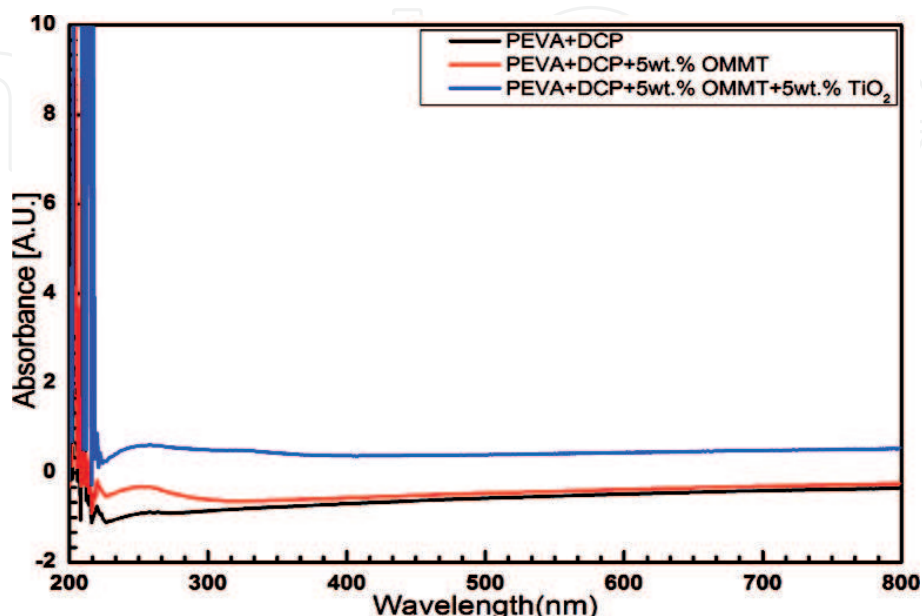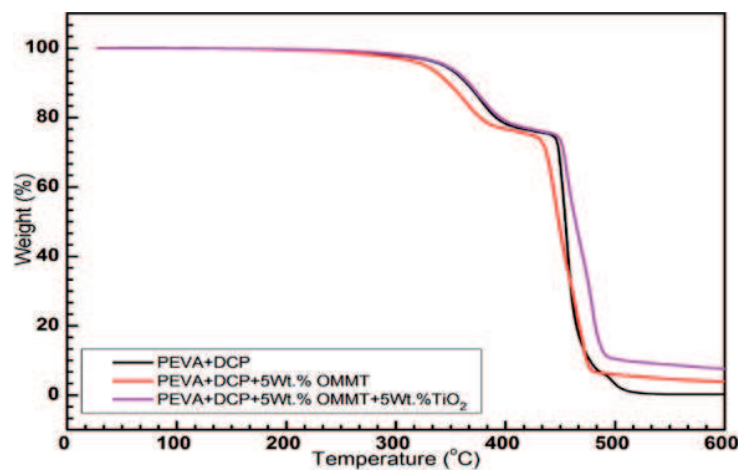

Figure 5.
*UV-Vis spectra of PEVA and nanocomposites.*

polyene [13, 14, 19, 20] taken place. Deacetylation occurs for all the samples in the temperature region between 300 and 400°C. After an inert or oxidative deacetylation of PEVA, a polyene is formed, further inert degradation of this polyene by chain scission processes, which could be neglected since for PV encapsulant application the maximum operating temperature is around 100°C [20]. The TGA thermographs assured the degradation of the hybrid nanocomposite at a higher temperature (around 420°) with faster rate as high transparency was observed form the UV-Vis spectrum.

3.6 Dielectric constant (ε')

Figure 7 shows the variation of dielectric constant (ε') with the frequency and loading of OMMT and TiO$_2$ nanofillers. The dielectric constant decreases up to 10^4 Hz above which it increases over the measured frequency range up to 10^6 Hz in neat PEVA, PEVA + 5 wt.% OMMT and PEVA + 5 wt.% OMMT + 5 wt.% TiO$_2$ nanocomposite samples. The decrease of dielectric constant with frequency in neat PEVA may be attributed to the fact that at a low-frequency dielectric constant for the polar material is due to the contribution by various polarizations namely, electronic, ionic, orientational and interfacial polarization. The resulting total polarization in dielectric materials is due to sum of these four types of polarization [21]. The polarization contribution due to dipole orientation dominates at low frequencies.

Figure 6.
TGA thermograms of PEVA and nanocomposites.
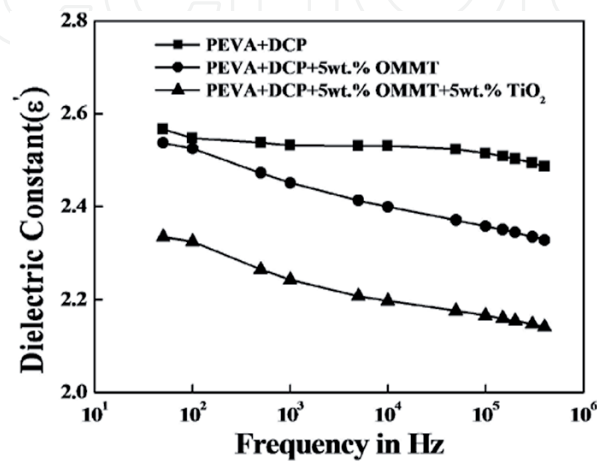
Figure 7.
Plot of dielectric constant of neat PEVA, PEVA + OMMT and PEVA + OMMT + TiO$_2$ nanocomposites with frequency.

The speed of dipole rotation at high frequency is insufficient to match the shift in the applied AC bias [22].

The plot of dielectric constant (ε') with frequency of PEVA + 5 wt.% OMMT nanocomposite might be understood by that the clay in exfoliated/intercalated form within the polymer matrix has terminated the regular long chains of the polymer and the resulting polymer structure is more random with shorter chains. Within the polymer due to nanoconfinement of the clay, dipole orientation may be constrained and not easily moved. The nanoscopic confinement effect from layered silicate inorganic hosts was reported by Anastasiadis et al. [23]. The author reported that X-ray diffraction showed that the polymer is confined within 1.5–2.0 nm. This confinement effect is directly reflected in the local reorientational dynamics. We believed that the orientation polarization is thus largely reduced due to this randomly distributed and confined structure within the polymer. It is observed that with the addition of OMMT nanofillers the dielectric constant in PEVA polymer decreases. The changes in the dielectric constant values of polymer clay nanocomposites (PCNs) have a strong correlation with intercalated/exfoliated structures of OMMT in the polymer matrix [24, 25]. It has been established that for the PCNs, the dielectric constant decreases due to the predominance of exfoliated-OMMT structure in a polymer matrix, whereas it increases for a large amount of intercalated structure [25–29].

It is also evident from **Figure** 7, that with the addition of 5 wt.% TiO$_2$ nanofiller to PEVA-OMMT nanocomposite sample with 5 wt.% OMMT, the dielectric constant increases. This increase in dielectric constant of nanocomposite sample with the addition of 5 wt.% TiO$_2$ is due to TiO$_2$ exhibits strong ionic polarization due to Ti^{4+} and O^{2-} ions and hence PEVA nanocomposite with TiO$_2$ filler has higher value of dielectric constant [30]. The polarization mechanism in nano-TiO$_2$ and OMMT over the frequency studied are closely identical, and therefore the resulting trends in the dielectric constant variations in both the nanocomposites are expected to be similar. The effective dielectric constant with TiO$_2$ is always higher than the values obtained with OMMT as nanofiller. This result may be due to (i) nanofiller inherent dielectric constant, and (ii) nanofiller concentration. TiO$_2$ has a higher dielectric constant than OMMT and hence the effective dielectric constant increases with the addition of TiO$_2$ and is always higher than PEVA + 5 wt.% OMMT nanocomposites. The other aspect is, since the density of OMMT (density ≈ 1.9 g/cm^3) is less than that of TiO$_2$ (density ≈ 4.2 g/cm^3), for the same quantum of loading, the PEVA nanocomposite with OMMT as a nanofiller will have more number of OMMT nanoparticles as compared to TiO$_2$ nanoparticles. With fillers in nanometer scales, this difference in the number of particles can be very significant. Thus, for a fixed filler loading, OMMT nanofillers in the PEVA nanocomposite films will introduce more interfaces causing additional restrictions to the polymer chain mobility when compared to TiO$_2$ nanofillers. This enhanced chain mobility restrictions with OMMT nanofillers coupled with the effect of a lower OMMT dielectric constant, will lead to lowering of effective dielectric constant of PEVA + 5 wt.% OMMT nanocomposite, to values lower than that of the TiO$_2$ filled ones. Although both these processes will be dynamic in the nanocomposites and also it is difficult to segregate their individual contributions. Further, the variations in dielectric constant are not linear with respect to filler loading. However, there are indications of existence of a threshold value of filler loading at which the dielectric constant shows maximum variation with respect to base polymer PEVA values [31].
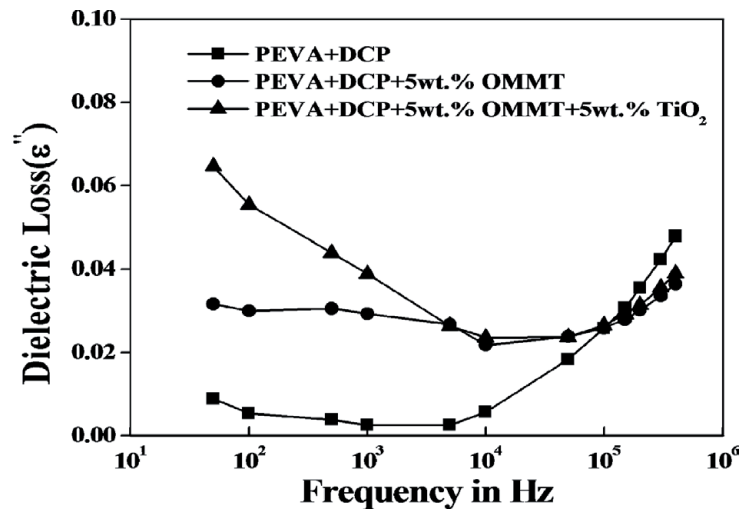
3.7 Dissipation factor (tanδ)

Figure 8 shows the variation of dissipation factor (tanδ) of neat PEVA, PEVA + 5 wt.% OMMT, and PEVA + 5 wt.% OMMT + 5 wt.% TiO$_2$ nanocomposites
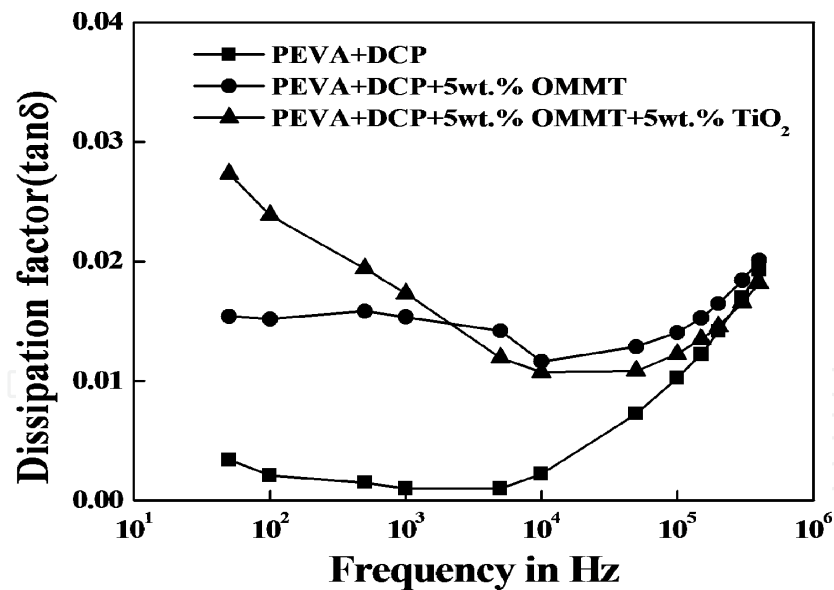
Figure 8.
Plot of dissipation factor (tanδ) of neat PEVA, PEVA + OMMT and PEVA + OMMT + TiO₂ nanocomposites with frequency.

Figure 9.
Plot of dielectric loss (ε") of neat PEVA, PEVA + 5 wt.% OMMT and PEVA + 5 wt.% OMMT + 5 wt.% TiO₂ nanocomposites with frequency.

with respect to frequency. The dissipation factor decreases with increase in frequency in low-frequency range up to 10^4 Hz and above which it increases with increase in frequency. Though there is an increase in tanδ in a high-frequency range beyond 10^4 Hz the dissipation factor values are well within the acceptable range and no substantial increase. It is observed that with the addition of nanofillers the dissipation factor increases in PEVA polymer.

The dissipation factor variations of PEVA nanocomposites are dependent on the frequency of the applied voltage and the temperature of measurement. Therefore the temperature of the measurement was maintained constant. The dissipation factor depends on the electrical conductivity of polymer nanocomposites. The electrical conductivity in turn depends on the number of charge carriers in the bulk of the material, the relaxation time of the charge carriers and the frequency of the applied electric field. Since the measurement temperature is maintained constant, its influence on the relaxation times of the charge carriers is neglected. Over the range of frequency used, charge transport therefore is dominated by the lighter electronic charge carriers.

11

3.8 Dielectric loss (ε')

Figure 9 shows the variation of dielectric loss (ε'') of neat PEVA, PEVA + 5 wt.% OMMT and PEVA + 5 wt.% OMMT + 5 wt.% TiO_2 nanocomposites with frequency and nanofillers. It is observed that increase in dielectric loss with the addition of nanofillers in PEVA polymer and the increases with frequency beyond 10^5 Hz in neat PEVA, PEVA + 5 wt.% OMMT and PEVA + 5 wt.% OMMT + 5 wt.% TiO_2 nanocomposites. Beyond 10^5 Hz dielectric loss in nanocomposites has reduced as compared to that of neat PEVA. Loss factor in nanocomposites might be the contribution from dipole orientation, conduction loss and interfacial polarization [32]. The measurement results of dielectric loss are helpful to confirm the polarization mechanism. The loss factor ε'' of composite systems could be expressed as a sum of three distinct contributions [32], that is,

$$\varepsilon'' = \varepsilon''_{dc} + \varepsilon''_{MW} + \varepsilon''_{D} \tag{1}$$

where ε''_{dc} is due to conduction loss contribution, ε''_{MW} is due to interfacial polarization (Maxwell-Wagner) contribution and ε''_{D} is the dipole orientation or Debye loss factor. The conduction loss and interfacial polarization loss factors are expressed as $\varepsilon''_{dc} = \sigma_{dc}$.

$$\varepsilon''_{dc} = \frac{\sigma_{dc}}{2\pi f \varepsilon_0} \tag{2}$$

$$\varepsilon''_{MW} = \varepsilon_\infty \left(1 + \frac{K}{1 + (2\pi f)^2 \tau^2} \right) \tag{3}$$

ε_∞ and K are calculated considering two different dielectric constants of the sample at the interfaces and τ is the relaxation time of the interfacial polarization. ε_0 and f are the dielectric constant of vacuum and frequency, respectively. By expressing Eqs. (2) and (3) in logarithmic form and plotting log ε''_{dc} and log ε''_{MW} versus log f, we can obtain two different curves: the log ε''_{dc} against log f represents a straight line and the log ε''_{MW} against log f represents a sigmoidal curve. From **Figure 9**, it is evident that, at high frequencies, a broad loss peak appears. This broad loss peak corresponds to the dipole orientation polarization. At low frequency-range, the plot shows a straight line indicating the existence of conduction loss.

4. Conclusions

This study shows that a fair degree of success has been achieved in production of pristine PEVA base and organically modified nanoclay (OMMT) and TiO_2 added nanocomposite films. The pristine PEVA and organically modified nanoclay (OMMT) and titania (TiO_2) added nanocomposite films have been analyzed by series of tests. The following conclusions were drawn from the research work:

i. The XRD results indicate that the absence of the characteristic peak indicates the exfoliation of the OMMT platelets in the Epoxy matrix.

ii. The SEM micrographs indicate that the nanofillers were uniformly distributed and good adhesion between PEVA polymer and nanofillers.

iii. The FTIR spectra of nanocomposite films show the characteristic transmittance bands of pristine PEVA and OMMT + TiO_2 nanofillers. The existence

of a chemical interaction (formation of hydrogen bond) between nanofillers and polymer chains of the PEVA and nanocomposite films has been established through Fourier Transform Infrared spectroscopy.

iv. From the UV-Vis, it was confirmed that there is a decrease in UV transmission of PEVA and retained a high visible light transmission. Therefore, these nanocomposite films with light selective properties would be an excellent component for PV encapsulation.

v. The TGA thermographs assured the degradation of the hybrid nanocomposite at a higher temperature (around 420°) with faster rate as high transparency was observed from the UV-Vis spectrum.

vi. The results of dielectric constant and tanδ of nanocomposites with respect to frequency, nanofiller concentrations, were interesting and intriguing. The frequency and filler dependant dielectric constant characteristics of PEVA and nanocomposites films suggest that there is an inhibition in the mobility of PEVA polymer chains in the bulk of the nanocomposites.

vii. The dissipation factor variation with respect to frequency and filler loading indicate that there is probably a reduction in electrical conductivity in nanocomposites. This is mainly due to inhibition in the mobility of available charge carriers. Though there is an increase in tanδ in a high-frequency range beyond 10^4 Hz the dissipation factor values are well within the acceptable range and no substantial increase.

viii. Some encouraging results such as decrease in dielectric loss, dissipation factor and dielectric loss with the addition of nanofillers, indicates that the nanocomposite films can be used as solar encapsulants. The UV-vis result also indicates that the nanocomposites films are transparent to light in the range between 200 and 800 nm and insights are gained for understanding of the polarization mechanisms involved.

Author details

Rashmi Aradhya*, Madhu Bilugali Mahadevaswamy and Poornima

Department of Electrical and Electronics Engineering, Siddaganga Institute of Technology, Tumkur, Karnataka, India

*Address all correspondence to: rash_mysore@sit.ac.in; rash_mysore@yahoo.com

IntechOpen

References

[1] I. E. Agency. World Energy Outlook 20132013. DOI: 10.1787/weo-2013-en

[2] Hanemann T, Szabó DV. Polymer-nanoparticle composites: From synthesis to modern applications. Materials. 2010;**3**(6):3468-3517. DOI: 10.3390/ma3063468

[3] Duquesne S, Jama C, Le Bras M, Delobel R, Recourt P, Gloaguen JM. Elaboration of EVA-nanoclay systems—Characterization, thermal behaviour and fire performance. Composites Science and Technology. 2003;**63**(8):1141-1148. DOI: 10.1016/S0266-3538(03)00035-6

[4] Alexandre M, Dubois P. Polymer-layered silicate nanocomposites: Preparation, properties and uses of a new class of materials. Materials Science & Engineering R: Reports. 2000;**28**(1):1-63. DOI: 10.1016/S0927-796X (00)00012-7

[5] Jeon IY, Baek JB. Nanocomposites derived from polymers and inorganic nanoparticles. Materials. 2010;**3**(6):3654-3674. DOI: 10.3390/ma3063654

[6] Kango S, Kalia S, Celli A, Njuguna J, Habibi Y, Kumar R. Surface modification of inorganic nanoparticles for development of organic-inorganic nanocomposites—A review. Progress in Polymer Science. 2013;**38**(8):1232-1261. DOI: 10.1016/j.progpolymsci.2013.02.003

[7] Lü C, Yang B. High refractive index organic-inorganic nanocomposites: design, synthesis and application. Journal of Materials Chemistry. 2009;**19**(19):2884. DOI: 10.1039/b816254a

[8] Tcherbi-Narteh A, Hosur M, Triggs E, Owuor P, Jelaani S. Viscoelastic and thermal properties of full and partially cured DGEBA epoxy resin composites modified with montmorillonite nanoclay exposed to UV radiation. Polymer Degradation and Stability. 2014;**101**(1):81-91. DOI: 10.1016/j.polymdegradstab.2013.12.033

[9] Agroui K, Collins G, Oreski G, Boehning M, Arab AH, Ouadjaout D. Effect of crosslinking on EVA-based encapsulant properties during photovoltaic module fabrication process. Revue des Energies Renouvelables. 2015;**18**(2):303-314

[10] Fernández AI, Haurie L, Formosa J, Chimenos JM, Antunes M, Velasco JI. Characterization of poly(ethylene-co-vinyl acetate) (EVA) filled with low grade magnesium hydroxide. Polymer Degradation and Stability. 2009;**94**(1):57-60. DOI: 10.1016/j.polymdegradstab.2008.10.008

[11] Mishra SB, Luyt AS. Effect of organic peroxides on the morphological, thermal and tensile properties of EVA-organoclay nanocomposites. Express Polymer Letters. 2008;**2**(4):256-264. DOI: 10.3144/expresspolymlett.2008.31

[12] Zhang W, Chen D, Zhao Q, Fang Y. Effects of different kinds of clay and different vinyl acetate content on the morphology and properties of EVA/clay nanocomposites. Polymer. 2003;**44**(26):7953-7961. DOI: 10.1016/j.polymer.2003.10.046

[13] Wang KH, Choi MH, Koo CM, Choi YS, Chung IJ. Synthesis and characterization of maleated polyethylene/clay nanocomposites. Polymer. 2001;**42**(24):9819-9826. DOI: 10.1016/S0032-3861(01)00509-2

[14] Ugel E, Giuliano G, Modesti M. Poly (ethylene-co-vinyl acetate)/clay nanocomposites: Effect of clay nature

and compatibilising agents on morphological thermal and mechanical properties. Soft Nanoscience Letters. 2011;**01**(04):105-119. DOI: 10.4236/ snl.2011.14018

[15] Abhilash V, Rajender N, Suresh K. X-ray diffraction spectroscopy of polymer nanocomposites. In: Spectroscopy of Polymer Nanocomposites. Elsevier; 2016. pp. 410-451. DOI: 10.1016/ B978-0-323-40183-8.00014-8

[16] Zanetti M, Camino G, Thomann R, Mülhaupt R. Synthesis and thermal behaviour of layered silicate-EVA nanocomposites. Polymer. 2001;**42**(10):4501-4507. DOI: 10.1016/ S0032-3861(00)00775-8

[17] Bagheri S, Shameli K, Abd Hamid SB. Synthesis and characterization of anatase titanium dioxide nanoparticles using egg white solution via sol-gel method. Journal of Chemistry. 2013;**2013**:5. DOI: 10.1155/2013/848205

[18] Rimez B, Rahier H, Van Assche G, Artoos T, Biesemans M, Van Mele B. The thermal degradation of poly(vinyl acetate) and poly(ethylene-co-vinyl acetate), part I: Experimental study of the degradation mechanism. Polymer Degradation and Stability. 2008;**93**(4):800-810. DOI: 10.1016/j. polymdegradstab.2008.01.010

[19] Rimez B, Rahier H, Van Assche G, Artoos T, Van Mele B. The thermal degradation of poly(vinyl acetate) and poly(ethylene-co-vinyl acetate), part II: Modelling the degradation kinetics. Polymer Degradation and Stability. 2008;**93**(6):1222-1230. DOI: 10.1016/j. polymdegradstab.2008.01.021

[20] Pramanik M, Srivastava SK, Samantaray BK, Bhowmick AK. EVA/ clay nanocomposite by solution blending: Effect of aluminosilicate layers on mechanical and thermal

properties. Macromolecular Research. 2003;**11**(4):260-266. DOI: 10.1007/ BF03218362

[21] Barsoum MW. Fundamentals of Ceramics. 2003. DOI: 10.1887/0750309024

[22] Davies JT. Dielectric Behaviour and Structure. New York: McGraw-Hill Book Company, Inc; 1955. pp. 199-200. DOI: 10.1016/0009-2509(56)80047-X

[23] Anastasiadis SH, Karatasos K, Vlachos G, Manias E, Giannelis EP. Nanoscopic-confinement effects on local dynamics. Physical Review Letters. 2000;**84**(5):915-918. DOI: 10.1103/ PhysRevLett.84.915

[24] Wang H-W, Dong R-X, Liu C-L, Chang H-Y. Effect of clay on properties of polyimide-clay nanocomposites. Journal of Applied Polymer Science. 2007;**104**(1):318-324. DOI: 10.1002/ app.25740

[25] Bershtein VA et al. Polycyanurate-organically modified montmorillonite nanocomposites: Structure-dynamics-properties relationships. Journal of Macromolecular Science, Part B Physics. 2008;**47**(3):555-575. DOI: 10.1080/00222340801955545

[26] Sengwa RJ, Sankhla S, Choudhary S. Dielectric characterization of solution intercalation and melt intercalation polyvinyl alcohol-poly(vinyl pyrrolidone) blend-montmorillonite clay nanocomposite films. Indian Journal of Pure and Applied Physics. 2010;**48**(3):196-204. DOI: 10.1016/j. compscitech.2010.06.003

[27] Sengwa RJ, Choudhary S, Sankhla S. Dielectric properties of montmorillonite clay filled poly(vinyl alcohol)/poly(ethylene oxide) blend nanocomposites. Composites Science and Technology. 2010;**70**(11):1621-1627. DOI: 10.1016/j.compscitech.2010.06.003

[28] Sengwa RJ, Choudhary S. Investigation of correlation between dielectric parameters and nanostructures in aqueous solution grown poly(vinyl alcohol)-montmorillonite clay nanocomposites by dielectric relaxation. Spectroscopy. 2010. DOI: 10.3144/expresspolymlett.2010.70

[29] Zhang LD, Zhang HF, Wang GZ, Mo CM, Zhang Y. Dielectric behaviour of nano-TiO_2 bulks. Physica Status Solidi. 1996;**157**(2):483-491. DOI: 10.1002/pssa.2211570232

[30] Nelson JK, Fothergill JC. Internal charge behaviour of nanocomposites. Nanotechnology. 2004;**15**(5):586-595. DOI: 10.1088/0957-4484/15/5/032

[31] Brosseau C, Achour ME. Variable-temperature measurements of the dielectric relaxation in carbon black loaded epoxy composites. Journal of Applied Physics. 2009;**105**(12):124102. DOI: 10.1063/1.3149702

[32] Fattoum A, Gmati F, Bohli N, Arous M, Mohamed AB. Effects of the matrix molecular weight on conductivity and dielectric relaxation in plasticized polyaniline/polymethylmethacrylathe blends. Journal of Physics D: Applied Physics. 2008;**41**(9):95407. DOI: 10.1088/0022-3727/41/9/095407

We are IntechOpen,
the world's leading publisher of
Open Access books
Built by scientists, for scientists

6,300
Open access books available

171,000
International authors and editors

190M
Downloads

154
Countries delivered to

Our authors are among the

TOP 1%
most cited scientists

12.2%
Contributors from top 500 universities

BOOK CITATION INDEX
CLARIVATE ANALYTICS
INDEXED

WEB OF SCIENCE™

Selection of our books indexed in the Book Citation Index
in Web of Science™ Core Collection (BKCI)

Interested in publishing with us?
Contact book.department@intechopen.com

A Novel Sensing Method for VOCs Using Nanoparticle-Coated Nanoporous Silicon

Selvakumar Varadarajan Subramani, Suganthi Selvakumar and Sujatha Lakshminarayanan

Abstract

Structural aspects, such as grain size, pore size, and crack-free film morphology, of porous silicon (PS), etc., play a vital role in the sensing of volatile organic compounds (VOCs). This chapter discusses a novel method for sensing of VOCs using porous silicon coated with a layer of ZnO (PS-ZnO). It was noted that the sensing ability of the PS sensor has increased due to the transconductance mechanism, as a result of the coating of ZnO over PS. Initially, porous silicon is formed by electrochemical wet etching of silicon and by electrophoretic deposition (EPD), ZnO is coated over porous silicon. An increase in the selectivity is due to the increase in surface-to-volume ratio and uniformity in the pore structures. The thickness of ZnO layer can be tuned up to 25 nm by applying a DC voltage between the copper electrode and the conductive silicon substrate immersed in a suspension of ZnO quantum dots. The influence of quantum dot concentration on the final layer thickness was studied by X-ray diffraction (XRD). The change in resistance for ethanol was found to be 12.8–16 MΩ and 8–16 MΩ for methanol.

Keywords: porous silicon, VOC sensing, metal oxide coating, electrochemical wet etching

1. Introduction

Porous silicon (PS) is a vital medium, which can be fabricated easily by electrochemical etching of silicon in HF acid solution [1]. The surface area of PS can be up to million times than that of a planar silicon surface. The melting point of silicon is lowered due to this high surface area [2]. Due to its characteristics such as high surface area and high chemical activity, it is popularly used as sensors to detect gases like NO_2, NH_3, H_2S, SO_2, ethanol, and acetone [1–3]. Compared to other semiconductor-based gas sensors (SnO_2, CuO, Cr_2O_3, and V_2O_5), PS-based gas sensors operate at comparatively lower temperatures, even at room temperature (RT) [4]. Furthermore, PS manufactured by the semiconducting material is compatible with silicon IC technology that provides the possibility to integrate the PS-based sensing element into any device [4–6]. This makes PS a promising gas-sensing material. However, the poor sensitivity and low thermal stability limit the industrial applications of PS [7].

Zinc oxide (ZnO) as an instantaneous band gap semiconductor (E_g = 3.37 eV) is used in development of gas sensors, optoelectronic devices, photovoltaic devices, and piezoelectrics [5–8]. Recent observations by Rai et al. have shown that the sensing properties of sensors depend on the morphology and surface-to-volume ratio of the sensing materials [9]. It is believed that ZnO nanostructures have high sensitivity due to their high surface-to-volume ratio and high electron mobility [5–9]. They are already being used for sensing gases such as NO_2, H_2, CO, and ethanol [5–12]. ZnO can be prepared in RT through electrophoretic deposition (EPD) of a colloidal suspension of quantum debris. EPD has been widely used to deposit particles within the micron size [13, 14]. Moreover, compared with the other processing methods, EPD is able to produce uniform deposits with high microstructural homogeneity. This helps us to control the deposit thickness and in depositing coatings on a broad range of patterns [15–17]. However, the high operating temperature and high power consumption of ZnO-based gas sensors limit its application.

The presence of a certain gas can be detected by the change in resistance produced in the sensor due to the adsorption of the analyte molecules by the PS film [18, 19]. In this chapter, we have discussed the fabrication procedure and the sensing mechanism of VOCs by PS-based gas sensor coated with ZnO (PS-ZnO) nanoparticles. The sensitivity, selectivity, and repeatability of the PS-ZnO sensor are also discussed. The primary grail of this research is to bring up a competitive impedance metric analysis of a two-point metal contact on PS-ZnO-based VOC sensor.

2. Experimental setup

2.1 Fabrication of PS-ZnO-based VOC sensor

Figure 1 shows the cross-sectional view of PS-ZnO-based VOC sensor. Since the ethanol sensing mechanism involves the formation of two layers (ZnO and PS), the following steps are followed in the manufacturing process:

1. Surface planning or silicon wafer (10 ohm-cm) cleaning

2. Electrochemical wet etching of silicon

3. Formation of permeable silicon (couple of hundred nanometer)

4. Deposition of ZnO by electrophoretic deposition

5. Making Al contact terminals utilizing screen printing system

6. Constructing the test chamber for location of ethanol, alcohol, and methanol vapor utilizing potential analyzer

The first step in the manufacturing process involves the preparation or cleaning of the silicon wafer. It is done to expel the organic and inorganic impurities that may be present on the substrate. The standard procedure followed is the RCA clean method. It is a procedure that must be performed before electrochemical wet etching.

Initially in the RCA cleaning process, organic cleaning is used to remove the natural contaminants present in thesilicon. This process is called organic clean method. The chemicals used in the organic clean process are added in the ratio of 1:1:5 corresponding to $NH_4OH/H_2O_2/H_2O$. After the initial step, ionic impurities
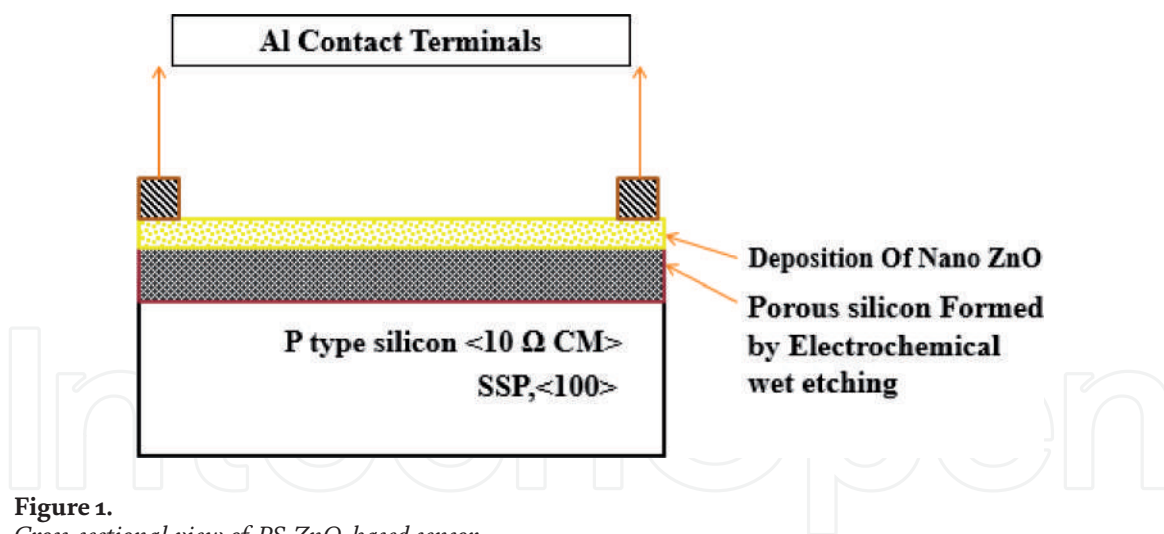
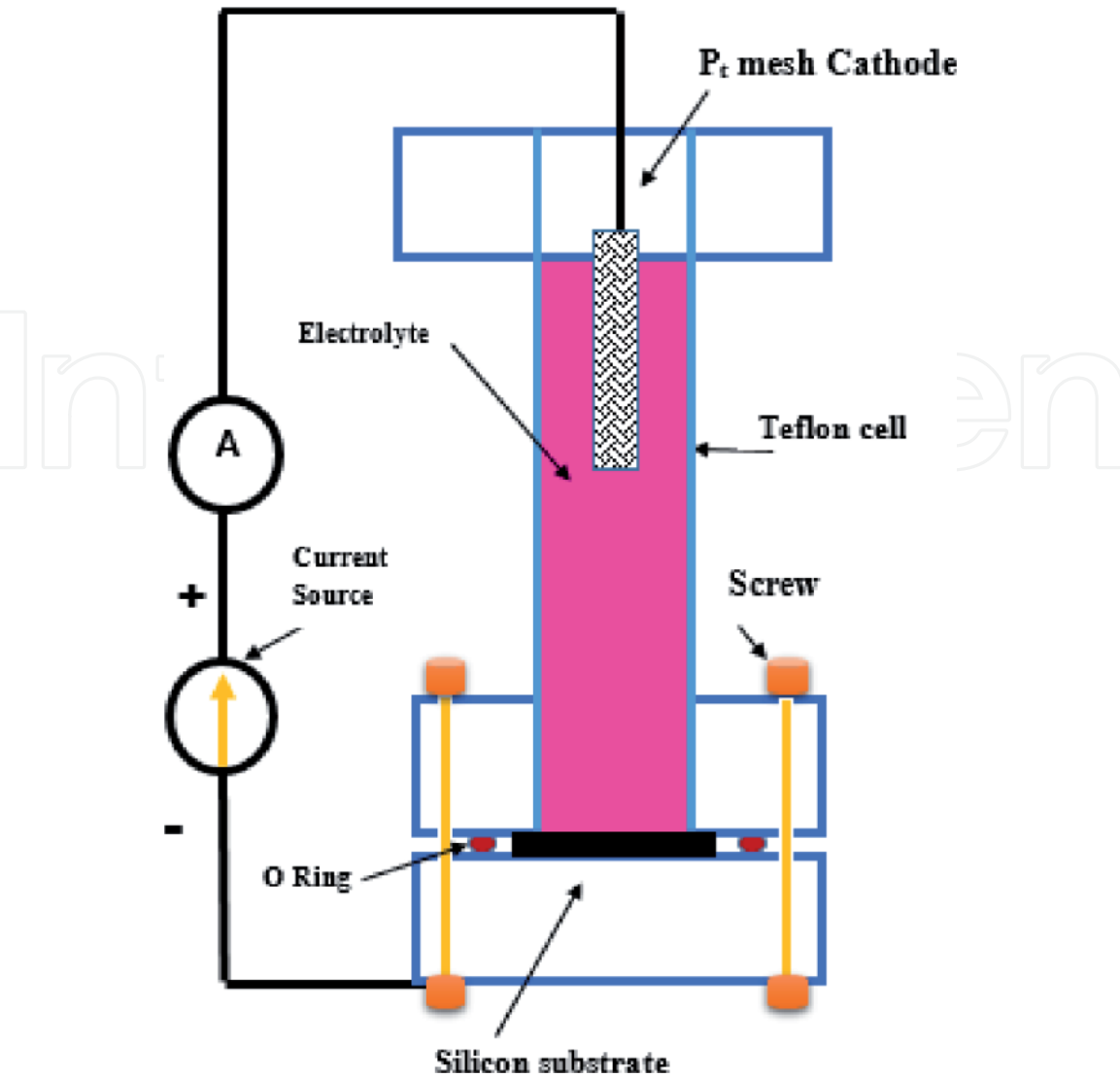**Figure 1.**
Cross-sectional view of PS-ZnO-based sensor.

(ionic pollutants) are removed by a process called ionic clean method. Here the cleaning solution is in the ratio 1:1:6 corresponding to $HCl/H_2O_2/H_2O$. Once the ionic impurities are removed, the wafer is washed with deionized (DI) water, and it is later dried with the help of N_2 gas. Now the wafer is submersed in a 1:50 arrangement of HF + H_2O at 75°C usually for 10 minutes, which helps to eliminate the thin oxide layer and some of the ionic contaminants. Finally, the wafer is again flushed in a solution of deionized water and dried again by nitrogen gas.

2.2 Formation of porous silicon (PS)

The second step is the manufacturing process in the formation of the porous silicon. The initial material is a solitary crystalline silicon of p-type substrate with 1–10 ohms-cm resistivity, <100> orientation, and 525 μm thickness and is polished on one side. Initially the surface cleaning process has been done as mentioned in the previous step in the manufacturing stream. After which, the wafers have been cut into rectangular bits of 2 × 2 cm to give a uniform current distribution over the surface of the substrate. A layer of aluminum is then deposited on the bottom the silicon specimen by means of thermal evaporation.

The experimental setup for the preparation of the porous silicon can be seen in **Figure 2**. Initially, the silicon sample has been put at the base of a round and hollow Teflon cell and is properly adjusted by a tempered steel plate which acts as a support material. The cell has two electrodes as shown. The silicon wafer is considered or used as an anode, and a platinum rod placed in a HF safe material is utilized as a cathode. In our trials, the Pt mesh which acts as the cathode was taken and set vertically opposite to the anode at the highest point of the cell. The space of the cell between the two electrodes is filled with the HF-based electrolyte. The electric flow is provided by the presence of a DC steady flow source which is used to connect the two electrodes. When there is a current flowing through the circuit, the cathode excites electrolytic solution which leads to the etching of numerous small pores on the surface of the anode (Si), thus leading to the formation of porous silicon.

The porosity of PS is proportional to the current density between the electrodes and the time of the process. To attain 65% porosity, it took up to 6 minutes at a current density of 5 mA/cm^2. To attain a porosity of 75%, in our case, it took 10 minutes at a current density of 15 mA/cm^2. After the successful formation of the porous silicon, the sample specimen was tested for photoluminescence by several experiments with ethanol and isopropyl alcohol.
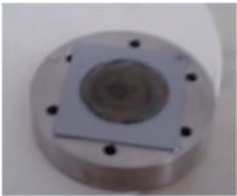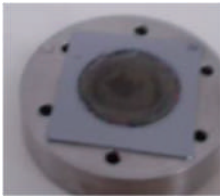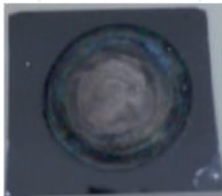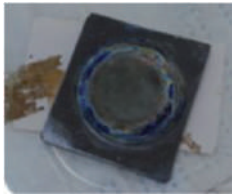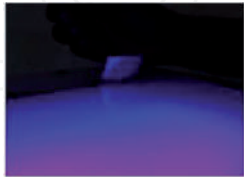
Figure 2.
Electrochemical wet etching of silicon.

From our observations described in the **Table 1**, we concluded that the photoluminescence property could be checked by the UV detection method. The UV photo illumination of porous silicon demonstrates that the reflected UV photography is excited by UV-transmitting LEDs or devices (radiation sources) or by solid daylight. A UV-transmitting channel is placed on the focal point, which enables bright light to pass and collects all visible and infrared light.

2.3 Selection of sensing materials

For optimal sensing performance, the sensing material to be selected should be carefully considered. The material selection is based on the operating temperature, range of detection, response time, sensing form, sensing parameters, and processing compatibility of the target VOC. Three materials—SnO_2, TiO_2, and ZnO—satisfy all the above parameters for the detection of VOC. However, among these three, ZnO operates at room temperature, which means that there is no need for a heating element. It also has a faster response time of less than a second and is silicon processing compatible. On the other hand, TiO_2 has a slow response time of about 3 minutes and operates only at 200–400°C. In addition, SnO_2 has a narrow range of detection and slower response time. The selectivity of SnO_2 is also less. Due to these reasons, we select ZnO as the sensing material.

S. No	Name	HF/ethanol	HF/IP	HF/IP	HF/IP
1.	P-type silicon	1	1	1	1
2.	Area	2.009 cm^2	2.009 cm^2	2.009 cm^2	2.009 cm^2
3.	Current density	5 mA/cm^2	5 mA/cm^2	7.5 mA/cm^2	10 mA/cm^2
4.	Current across anode and cathode	8 mA	10 mA	15 mA	20 mA
5.	Electrolyte	(3:7 (10 ml)	1:2 (10 ml)	1:2 (10 ml)	1:1(10 ml)
6.	Pt mesh cathode	1	1	1	1
7.	O ring	1	1	1	1
8	After experiment				
9	Photo luminance property checked by UV detection	No photo luminance	No photo luminance		

Table 1.
Different experimental results with photoluminescence.

2.4 Electrophoretic deposition of ZnO on PS

After the successful manufacturing of the porous silicon specimen, a thin layer of ZnO had to be deposited on the surface of the substrate by means of electrophoretic deposition (EPD). The mechanism of the EPD process is illustrated in **Figure 3**. A glass vessel was used for this experiment. The PS material to be coated was taken as the anode, and we utilized an aluminum rod as a cathode. The two electrodes were submerged in a solution of isopropanol which had numerous ZnO molecules suspended at the bottom of it. The apparatus had been equipped with a magnetic stirrer placed below the glass vessel which was used to stir the solution at high speeds. A DC voltage had been applied between the two electrodes which caused an electrochemical reaction between the two submerged electrodes. Initially, the suspended particles in the isopropanol were released due to the magnetic stirring process. Once the ZnO molecules start floating in the solution, the voltage caused the aluminum anode to repel the colloidal ZnO molecules, and the PS attracted them, causing a migration of particles from the positive to the negative anode, thus creating a thin layer of ZnO coating on it. After deposition, the samples were rinsed with deionized water and were air-dried with N_2 gas.

2.5 Experimental setup for VOC detection

The device was successfully fabricated and was tested for VOC detection. **Figure 4** shows the experimental setup of VOC detection by using PS-ZnO. The testing phase was conducted in an enclosed testing chamber. The specimen to be examined (PS-ZnO) was placed inside, and the chamber was tightly sealed. The chamber had been equipped with an electronic temperature controller attached to it, which regulates the temperature inside the chamber with the help of a heater coil wound around the chamber. The temperature of the coil was measured as well by means of an external thermometer to compare the actual temperature with the regulatory temperature.
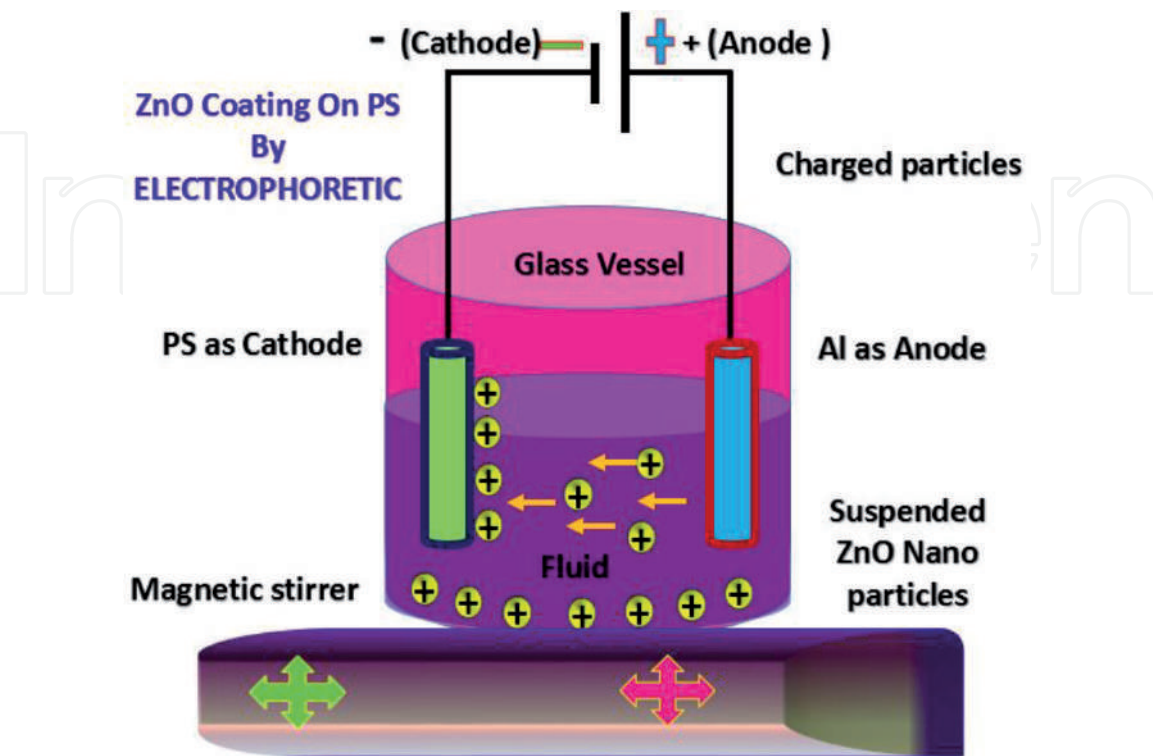
Figure 3.
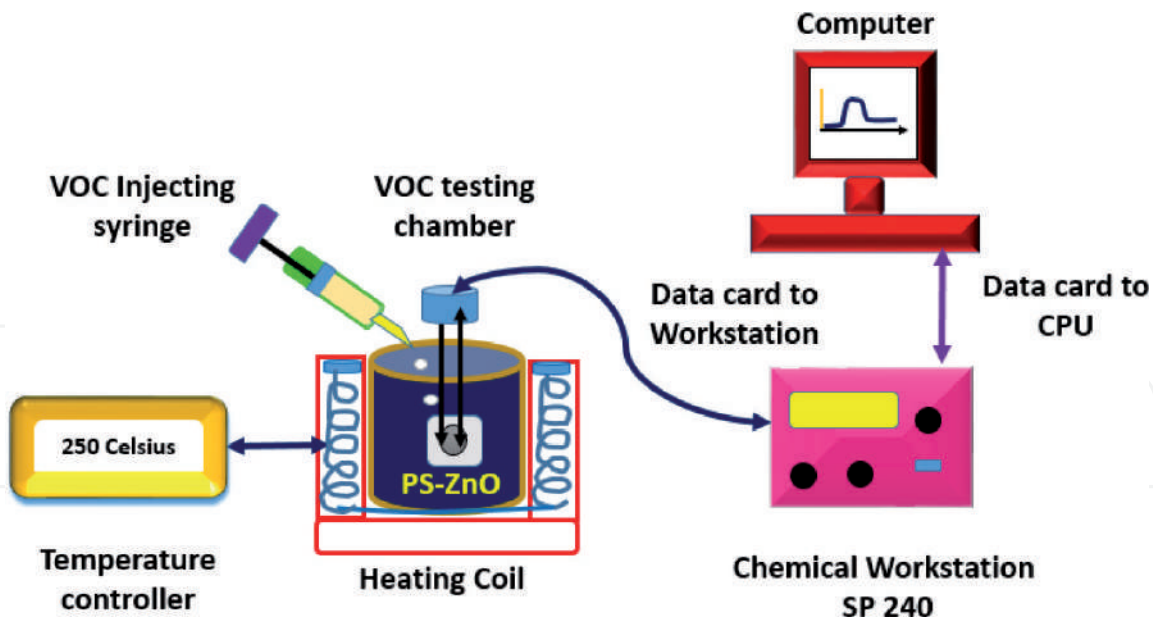*Illustration of the cathodic electrophoretic deposition process.*

Figure 4.
VOC recording system through chemical workstation.

For our study we had set the regulated temperature in the chamber to 250°C. A data cord was then connected from the testing chamber to a chemical workstation (SP 240). The chemical workstation was then further connected to a CPU to observe readings. The VOC compound to be tested was taken in a syringe and was slowly injected into the gas testing chamber. The injection of the compound was done in a gradual manner, and the corresponding data (impedance characteristics) on the display were observed and noted.

3. Results and discussion

The pictures below in **Figure 5(a)** and **(b)** show the structure of porous silicon before and after the electrophoretic deposition of ZnO on its surface, respectively. The images were used to illustrate the basic topological differences in appearance and structure of the PS substrate between the two stages. The microscopic images of micro PS samples shown in **Figure 6** were used to study the morphology of the substrate after the addition of the ZnO layer. The bright-field microscopic images clearly show
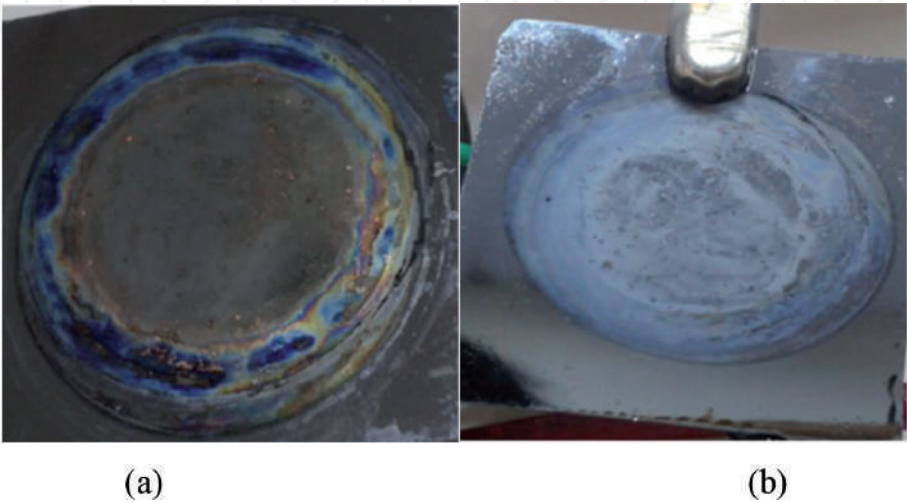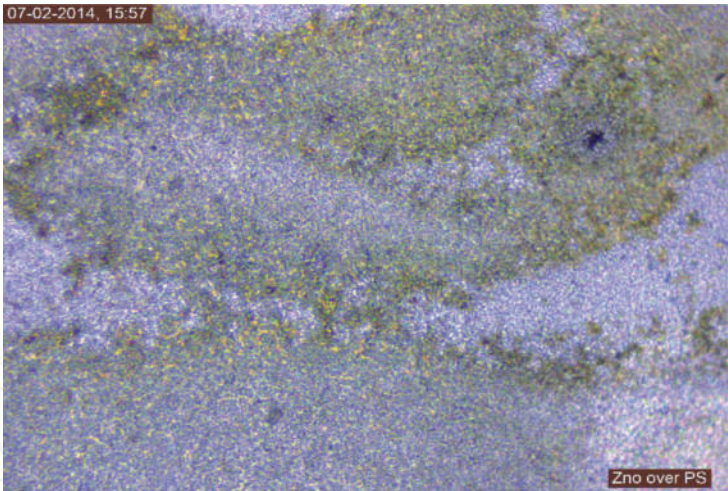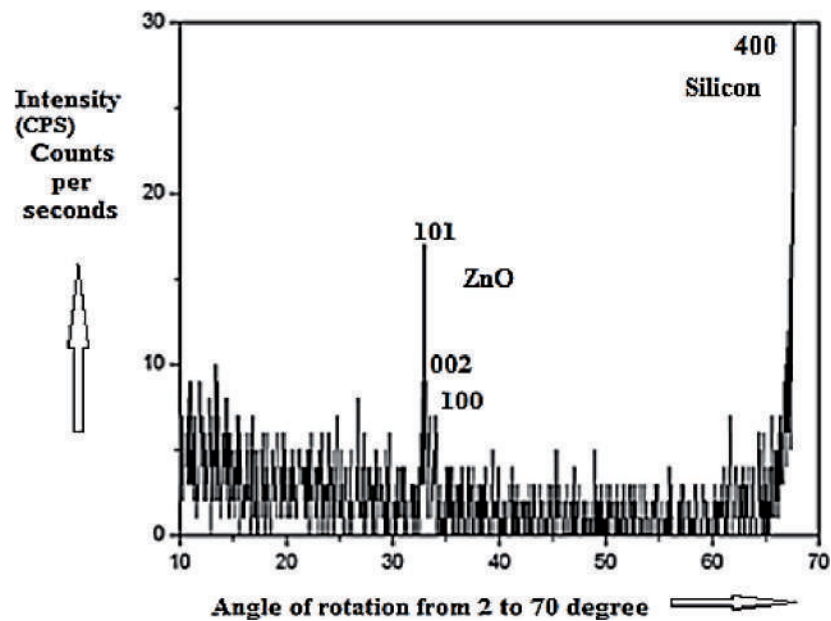

(a)   (b)

Figure 5.
(a) PS before ZnO deposition by EPD; (b) PS after deposition of ZnO by EPD.

Figure 6.
*Microscopic image of PS with ZnO.*

Figure 7.
XRD conformation of ZnO and silicon.

the structural changes in the obtained porous silicon after the coating of ZnO by EPD process. It is observed that the pore sizes are in the order of nanometers. In addition, the pores in micro PS are random in nature with uniform deposition of ZnO.

The coating characterization of the device was tested using spectrum diffraction analysis of both the materials. **Figure 7** shows the conformed X-ray diffraction (XRD) spectrogram of ZnO nanoparticles that are coated on the surface of the PS substrate. Crystalline form of ZnO and PS was taken for the spectrum analysis, and the intensity characteristics were studied by varying the angle of rotation between 2 and 70°. Distinctive intensity peaks of ZnO and the porous silicon material were observed at 32°90′ and 69°8′, respectively. We also observed that the intensity in counts per second (CPS) was much higher for the porous silicon (400) compared to the deposited layer of the ZnO (101).

After studying the coating characterization of ZnO, the sensitivity and the responsivity of the sensor were studied. An impedance study was done with the ZnO-coated PS sensor for certain VOCs, namely, ethanol, isopropanol, and methanol. We also observed the rate-limiting processes that occur at particular frequencies during operation of the device in the impedance spectra.
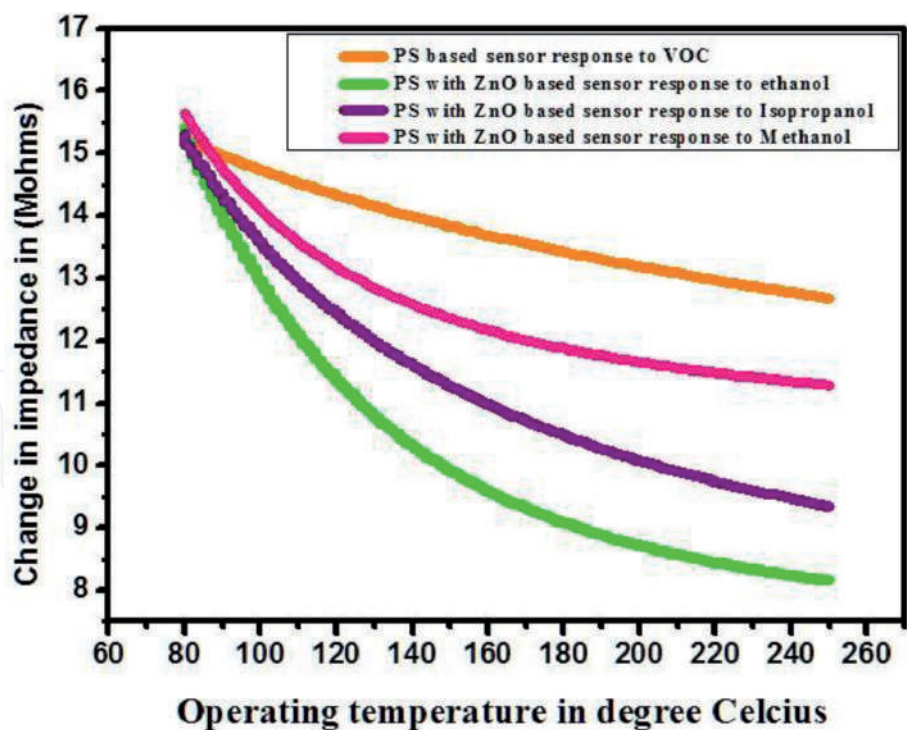
Figure 8.
Sensor response for ethanol, isopropanol, and methanol.

Figure 8 shows a typical Nyquist plot of data recorded from a PS-based sensor with an Al working electrode at room temperature. The plot also shows the results of two measurements made (resistance and temperature) when the sensor was exposed to three different VOCs: (1) ethanol, (2) methanol, and (3) isopropanol. **Figure 8** shows the measure of the change in resistance of the sensor at different temperatures ranging from 70–250°C. It was observed that the change in resistance varied from 8 to 15.8 MΩ for methanol and from 12 to 15.6 MΩ for isopropanol.

The measured change in resistance for ethanol was observed as well which varied from 12 to 15.8 MΩ at the same temperature gradient. We observed that the greatest percentage of change in the impedance measurement for the given temperature range was the highest for methanol. It is also evident that the percentage of change in resistance for the PS-based sensor without the ZnO coating is lower than the device coated with the ZnO film. The result thus proves that the sensing properties of a PS-based device are significantly increased by the addition of ZnO coating.

After observing the impedance characteristics of the device, we tested the responsivity of the sensor for different concentrations of ethanol. **Figure 9** shows the response of the ZnO-based VOC sensor for different concentrations of ethanol at a specific temperature of 250°C. We observed that as the concentration of ethanol kept increasing, the resistance of the device kept decreasing. This gave a linear increase in responsivity from 0 to 255 ppm of ethanol after which the increase in responsivity was relatively less due to saturation of ethanol level. After studying the sensitivity and responsivity of the sensor, the selectivity was studied as well.

Figure 10 summarizes the selectivity of PS toward aliphatic alcohol with respect to various VOCs at a frequency of 100 Hz. We observed that the selectivity of methanol was around 90%, while the same for ethanol and isopropanol compounds was around 50 and 60%, respectively. It shows that the response and recovery of the sensor are about 2 and 27 s, respectively. This indicates the response and recovery performance of the developed sensor toward methanol, ethanol, and isopropanol. The various quick responses and recoveries of methanol, ethanol, and isopropanol
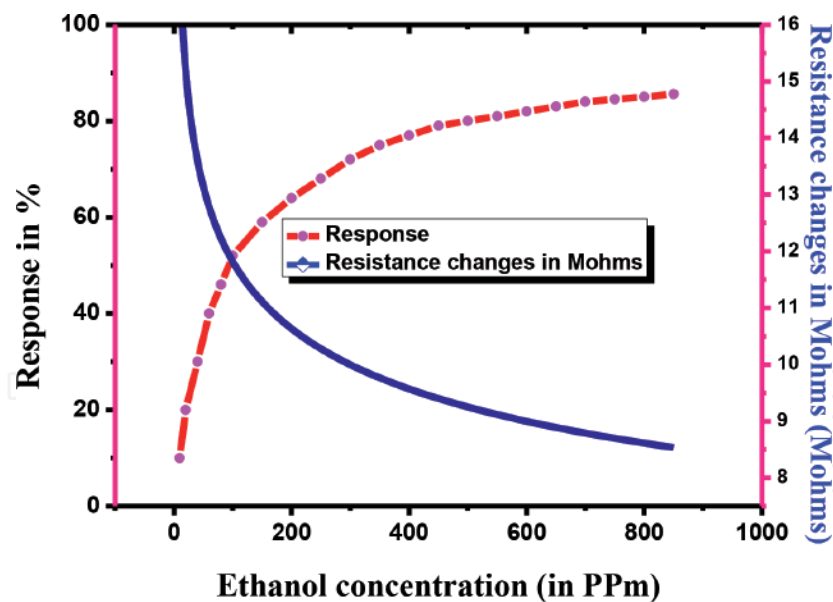
Figure 9.
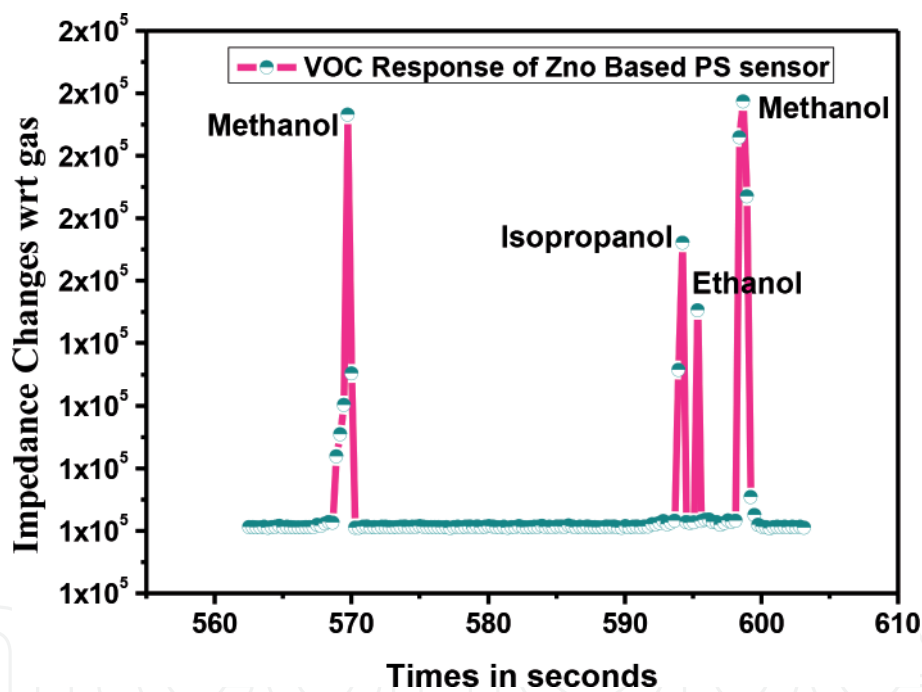*Response and sensitivity for ethanol concentration.*

Figure 10.
Sensor repeatability test for different VOC concentrations.

clearly prove selectivity of these VOCs by measuring different impedances. The ZnO-PS-based sensor is very sensitive to methanol when compared to all other VOCs.

From **Figure 11**, it is understood that the selectivity and repeatability are one of the range of acceptable values the sensor will read, relevant to a previous measurement, when measuring a methanol, ethanol, and isopropanol, independent of the actual gas concentration. It clearly shows that the sensing action remains unchanged for repeated measurement.

In the modern world, nanostructured oxide-based VOC sensors are used in applications such as monitoring the environment, chemical process control equipment, and health regulation devices. However, the crux of the operating mechanism is still not completely understood. Therefore, a deeper understanding would be beneficial to
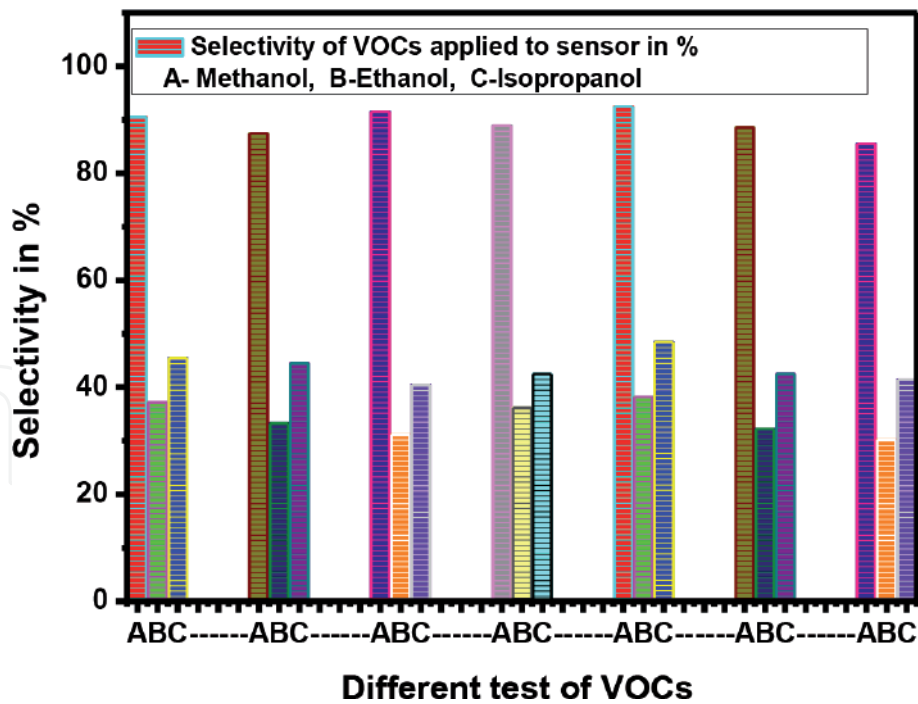
Figure 11.
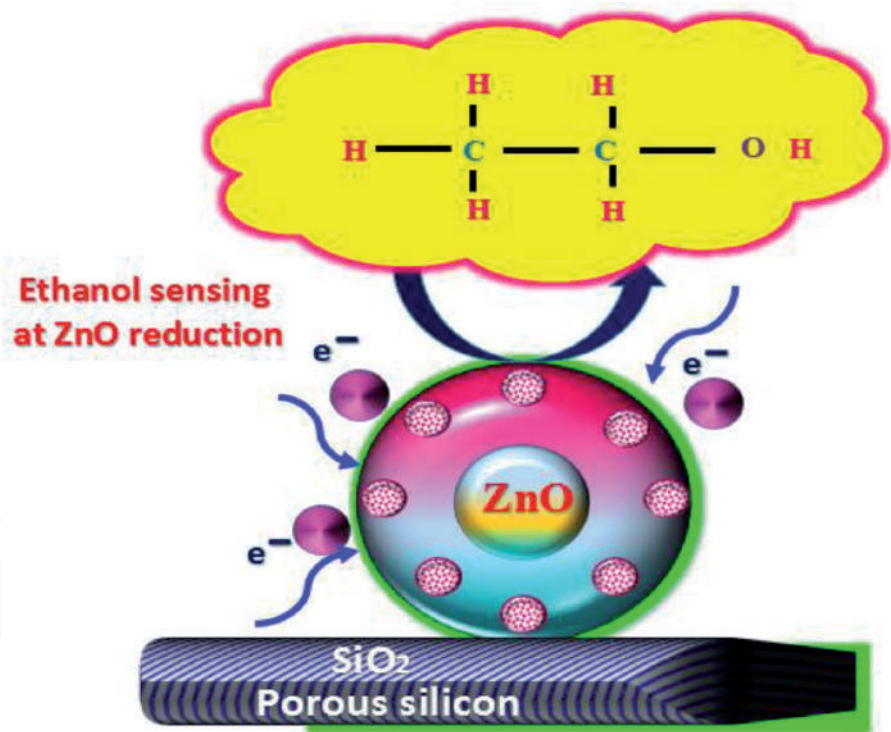*Sensor selectivity for VOC concentration in repeated test.*

Figure 12.
VOC sensing mechanism of ZnO-based PS sensor.

the development of enhanced sensing elements which can be used for the mentioned applications. In the case of ethanol sensing, our outcomes uncover that the focused adsorption of electrons at the nanostructure surfaces between the porous silicon and the ethanol particles via reduction process (as shown in **Figure 4**) indicates the presence of ethanol at that region. Therefore, the process of ethanol fixating on the ZnO can be identified electronically, helping us discover the sensing element.

Initially, there is an interaction between the ethanol molecules and the chemically absorbed oxygen ions that are present in the sensing element (ZnO). The
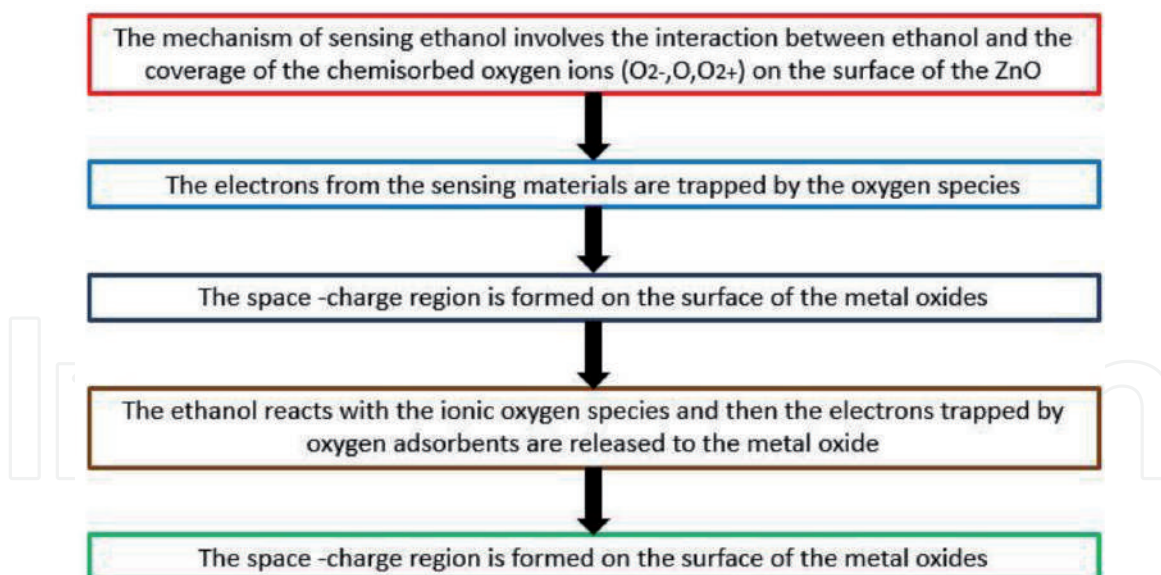
Figure 13.
VOC sensing mechanism of nanoparticle-based PS sensor.

electrons that are present in the sensing material are already trapped by these oxygen compounds or species. Due to this, a surface charge layer is formed on the surface of the metal oxide (ZnO). This in turn causes the ethanol to react with the ionic oxygen species that are present in the sensing material which leads to the release of the trapped electrons into the metal oxide. Finally, it reverts back to the space charge region on the surface of the metal oxide. **Figure 12** shows the graphical representation VOC sensing mechanism ZnO-based PS sensor; it clearly represents the reduction of ethanol (electron exchange with sensing layer) sensing mechanism of ZnO. The mechanism flow of sensing is expressed as a flow diagram in **Figure 13**.

4. Conclusion

The novel method for sensing of VOCs using a porous silicon sensor coated with a layer of ZnO has been presented. The key structural aspects have been explained in detail. The coating of ZnO over PS by EPD technique was carried out successfully. The XRD spectrography was used to successfully obtain distinct intensity peaks of 101 and 400 for ZnO and porous silicon which were found at 32.90 and 69.8, respectively. The resistance changes, which varied from 8 to 16 MΩ for methanol, 12 to 15.6 MΩ for isopropanol, and 12 to 15.8 MΩ for ethanol, were observed and studied carefully. This proved that device exhibited higher sensitivity and selectivity at the temperature range between 70 and 250°C for PS sensor coated with ZnO nanoparticles. We also concluded that the device works best for the sensing of ethanol as it showed high repeatability of up to 80% at saturated levels and has high selectivity of about 90% for methanol.

Acknowledgements

Author details

Selvakumar Varadarajan Subramani[1*] Suganthi Selvakumar[1] and
Sujatha Lakshminarayanan[1,2]

1 Department of Electronics and Communication Engineering, Rajalakshmi
Engineering college, Chennai, India

2 Centre of Excellence in MEMS and Microfluidics (CEMM), Rajalakshmi
Engineering College, Chennai, India

*Address all correspondence to: selvakumar.vs@rajalakshmi.edu.in

IntechOpen

References

[1] Razi F, Rahimi F, Irajizad A. Fourier transform infrared spectroscopy and scanning tunnelling spectroscopy of porous silicon in the presence of methanol. Sensors and Actuators B: Chemical. 2008;**132**(1):40-44

[2] Northen TR, Woo H-K, Northen MT, Nordström A, Uritboonthail W, Turner KL, et al. High surface area of porous silicon drives desorption of intact molecules. Journal of the American Society for Mass Spectrometry. 2007;**18**(11):1945-1949

[3] Ozdemir S, Gole JL. A phosphine detection matrix using nanostructure modified porous silicon gas sensors. Sensors and Actuators B: Chemical. 2010;**151**(1):274-280

[4] Ali NK, Hashim MR, Aziz AA. Effects of surface passivation in porous silicon as H_2 gas sensor. Solid-State Electronics. 2008;**52**(7):1071-1074

[5] Öztürk S, Kılınç N, altin NŢ, Öztürk ZZ. A comparative study on the NO_2 gas sensing properties of ZnO thin films, nanowires and nanorods. Thin Solid Films. 2001;**520**(3):932-938

[6] Balucani M, Nenzi P, Chubenko E, Klyshko A, Bondarenko V. Electrochemical and hydrothermal deposition of ZnO on silicon: From continuous films to nanocrystals. Journal of Nanoparticle Research. 2011;**13**:5985-5997

[7] Kanungo J, Saha H, Basu S. Pd sensitized porous silicon hydrogensensor-influence of ZnO thin film. Sensors and Actuators B: Chemical. 2010;**147**(1):128-136

[8] Chen YJ, Zhu C-L, Xiao G. Ethanol sensing characteristics of ambient temperature Nano chemically synthesized ZnO nanotubes. Sensors and Actuators B: Chemical. 2008;**129**(2):639-642

[9] Rai P, Raj S, Ko KJ, Park KK, Yu YT. Synthesis of flower-like ZnO microstructures for gas sensor applications. Sensors and Actuators B: Chemical. 2013;**178**(1):107-112

[10] Bai S, Sun C, Guo T, Luo R, Lin Y, Chen A, et al. Low temperature electrochemical deposition of nanoporous ZnO thin films as novel NO_2 sensors. Electrochimica Acta. 2013;**90**:530-534

[11] Bie LJ, Yan XN, Yin J, Duan YQ, Yuan ZH. Nano pillar ZnO gas sensor for hydrogen and ethanol. Sensors and Actuators B: Chemical. 2007;**126**(1):604-608

[12] Wan Q, Li QH, Chen YJ, Wang TH, He XL, Li JP, et al. Fabrication and ethanol sensing characteristics of ZnO nanowire gas sensors. Applied Physics Letters. 2004;**84**(18):3654

[13] Sarkar P, Nicholson PS. Electrophoretic deposition (EPD): Mechanism, kinetics and application to ceramics. Journal of the American Ceramic Society. 1996;**79**(1):1987-2002

[14] Boccaccini AR, Zhitomirsky I. Application of electrophoretic and electrolytic deposition techniques in ceramics processing. Current Opinion in Solid State & Materials Science. 2002;**6**(3):251-260

[15] Van der Biest OO, Vandeperre LJ. Electrophoretic deposition of materials. Annual Review of Materials Science. 1999;**29**:327-352

[16] Babsu S, Wang Y-h, Ghanshyam C, Kapur P. Fast response time alcohol gas sensor using nanocrystalline F-doped SnO_2 films derived via sol–gel method. Bulletin of Materials Science. 2013;**36**(4):521-533

[17] Jawad MJ, hashim MRR, Ali NK. Improvement of Al metal contact on porous silicon. Progress of Physics Research in Malaysia, AIP Conference Proceedings. 2010;**1250**(1):73-76

[18] Selvakumar VS, Sujatha L, Sundar R. Design analysis and electrical characteristics of porous silicon structure for sensor applications. Sensor Letters. 2018;**16**(4):1-6

[19] Selvakumar VS, Sujatha L, Sundar R. A novel MEMS microheater based alcohol gas sensor using nanoparticles. Journal of Semiconductor Technology and Science. 2018;**18**(4):445-453